UNIVERSITY OF CALIFORNIA
SANTA CRUZ

GEOPHYSICAL IDENTIFICATION OF SUBSURFACE WATER IN THE MCMURDO DRY VALLEYS REGION, ANTARCTICA

A dissertation submitted in partial satisfaction
of the requirements for the degree of

DOCTOR OF PHILOSOPHY

in

EARTH SCIENCES

by

Neil T. Foley

June 2020

The Dissertation of Neil T. Foley is approved:

_____
Professor Sławomir Tulaczyk, chair

_____
Professor Andrew Fisher

_____
Assistant Professor Terrence Blackburn

_____
Assistant Professor Myriam Telus

_____
Quentin Williams
Acting Vice Provost and Dean of Graduate Studies

Table of Contents

List of Figures

List of Tables

Abstract

Geophysical Identification of Subsurface Water in The McMurdo Dry Valleys Region, Antarctica

Neil T. Foley

In Antarctica, basic information about the shallow subsurface is difficult to determine due to logistical challenges, environmental concerns, and cover by ice and permafrost. The relative obscurity of the subsurface complicates answering basic geological questions such as:

- Is there water at depth? Does it harbor life? What is its origin? (Chapter 1)
- What is the chemistry of subsurface waters? Is there a hydrological and chemical connection across the landscape? (Chapter 2)
- How does heat flow through the subsurface? Where does melt occur? (Chapter 3)

In all of these questions, liquid water is a crucial component. Antarctica is unique among the continents in that nearly all its water is in the solid phase as ice. Even so, liquid water is widely found across the continent in the few places where pressure, heat flux and salinity permit the liquid phase. Liquid water and water ice typically have a strong electrical conductivity contrast due to water's ability to serve as a solvent with electrolytic properties. In the McMurdo Dry Valleys (MDV), a largely ice-free coastal zone, water typically contains a high solute load and so this contrast is exceptionally

high (Mikucki et al, 2015). The dissolved salts enable water to remain liquid at temperatures well below 0°C (Lyons et al, 2019).

We exploited this geophysical contrast to distinguish conductive subsurface brines from resistive ice, permafrost, and bedrock. We used a helicopter-borne Time Domain Electromagentic (TEM) system to measure resistivity in the shallow subsurface, ca. <500m below surface, in an initial 2011 survey (Mikucki et al, 2015; Foley et al 2015) and a follow up 2018 survey with an improved sensor (Foley et al, 2019). The TEM system works by inducing secondary EM currents in subsurface conductive materials; the decay of these currents is measured with a magnetometer. We inverted the recorded secondary magnetic field transients for a conductive layer model of the subsurface (see Auken et al, 2009; and Chapter 1). With this approach we mapped the transition from the frozen water ice near the Earth's surface to liquid water at depth.

We used this transition to map the subsurface brine's extent, and to estimate basic properties like salinity, temperature, and flux. In Chapter 1, we demonstrate that that groundwater is widely present at depths as shallow at 200m and temperatures around -10°C or warmer. The subsurface liquid water appears to be connected across wide areas in the MDV and potentially to a larger East Antarctic aquifer. In the MDV, it could possibly be connected to surface waters through sub-lake taliks, and it may also be connected to the ocean. In Chapter 2, improved data quality and a focus on the coastal zone all us to explore Darcian flow of this aquifer to the ocean. This pressure head gradient driven flow is just one of the suite of submarine groundwater discharge

(SGD) processes, but it is the only one that results in net flux of water from deep inland to the ocean (Santos et al, 2012). We use Chapter 2 to consider the MDV as a window into East Antarctic-wide SGD of a regional aquifer and estimate that slow SGD of such a concentrated brine may seed the coastal zone with gigagrams of bioavailable Fe and Si annually, comparable to other sources of nutrients to the coast.

A key factor determining the thickness of permafrost in the region is geothermal heat flux (GHF). In Chapter 3, we developed a new approach to using TEM data to estimate the flux in the study region, where it is not very well constrained. On Ross Island, we measured permafrost thickness and used this to estimate the local geothermal heat flux. Our calculations found a high, but reasonable heat flux of 90 mW/m^2 ±13 mW/m^2. A two-dimensional numerical model of heat conduction predicts high lateral heat flux from the relatively warm ocean into coastal permafrost, with implications for permafrost degradation and brine infiltration. The methods in Chapter 3 provide a blueprint for future GHF mapping with airborne TEM in the region and further afield.

Acknowledgements

The text of this dissertation includes reprints of the following previously published material:

Chapter 1:
Foley, N., Tulaczyk, S., Auken, E., Schamper, C., Dugan, H., Mikucki, J., Virginia, R., and Doran, P., 2015, Helicopter-borne transient electromagnetics in high-latitude environments: An application in the McMurdo Dry Valleys, Antarctica: Geophysics, v. 81, p. WA87–WA99, doi:10.1190/geo2015-0186.1.

Chapter 2:
Foley, N., Tulaczyk, M.S., Grombacher, D., Doran, T.P., Mikucki, J., Myers, F.K., Foged, N., Dugan, H., Auken, E., and Virginia, R., 2019, Evidence for Pathways of Concentrated Submarine Groundwater Discharge in East Antarctica from Helicopter-Borne Electrical Resistivity Measurements: Hydrology , v. 6, doi:10.3390/hydrology6020054.

Chapter 3:
Foley, N., Tulaczyk, S., Auken, E., Grombacher, D., Mikucki, J., Foged, N., Myers, K., Dugan, H., Doran, P.T., and Virginia, R.A., 2020, Mapping geothermal heat flux using permafrost thickness constrained by airborne electromagnetic surveys on the western coast of Ross Island, Antarctica: Exploration Geophysics, v. 51, p. 84–93, doi:10.1080/08123985.2019.1651618.

Foley was the primary author. Tulaczyk supervised. Schamper, Foged, Grombacher, and Auken provided instrumentation and processing. All authors contributed to grant writing and editing.

With deepest appreciation for co-authors' input, logistical support from Raytheon Polar Services / PHI Helicopters, and feedback from reviewers.

Thanks to William Altman. *Forsan et haec olim meminisse iuvabit.*

.

Chapter 1: Helicopter Borne Transient Electromagnetics in High Latitude Environments: An Application in The McMurdo Dry Valleys, Antarctica

ABSTRACT

The McMurdo Dry Valleys are a polar desert in coastal Antarctica where glaciers, permafrost, ice-covered lakes, and ephemeral summer streams coexist. Liquid water is found at the surface only in lakes and in the temporary streams that feed them. Past geophysical exploration has yielded ambiguous results regarding the presence of subsurface water. In 2011, we used a helicopter-borne, time-domain electromagnetic sensor to map resistivity in the subsurface across the Dry Valleys. The airborne electromagnetic (EM) method excels at finding subsurface liquid water in polar deserts, where water remains liquid under cold conditions if it is sufficiently saline, and therefore electrically conductive. Over the course of 26 hours of helicopter time we covered large portions of the Dry Valleys and vastly increased our geophysical understanding of the subsurface, particularly with respect to water. Our data show extensive subsurface low resistivity layers ~150-250m beneath higher resistivity layers, which we interpret as freeze-concentrated or 'cryoconcentrated' hypersaline brines lying beneath glaciers and frozen permafrost. These brines appear to be contiguous

with surface lakes, subglacial regions, and the Ross Sea, which could indicate a regional hydrogeologic system wherein solutes may be transported between surface reservoirs by ionic diffusion and subsurface flow. The presence of such brines underneath glaciers may have implications for glacier movement. Systems such as this, where brines exist beneath glacial ice and frozen permafrost, may exist elsewhere in coastal Antarctica; airborne EM resistivity is an ideal tool to find and survey them. Our application of time domain EM demonstrates that in polar subsurface environments containing conductive brines, such a diffusive electromagnetic method is superior to radar surveying in terms of depth of penetration and ability to differentiate hydrogeologic conditions.

INTRODUCTION

In polar regions, particularly in Antarctica, mean annual temperatures well below freezing shape the dominant physical and chemical landscape properties. The McMurdo Dry Valleys (MDV) form the largest ice-free region in Antarctica with mean annual temperatures of -15°C to -30°C (Doran *et al.*, 2002). The Transantarctic Mountains block the majority of ice from the East Antarctic Ice Sheet from entering several valleys, the largest of which open to the Ross Sea and are believed to have been fjords during the Miocene and Pliocene (Sugden *et al.*, 1995). The MDV are an example of an extreme polar desert, with minimal precipitation and high rates of moisture loss through wind-driven ablation and sublimation (Doran *et al.*, 2002). Despite the cold and arid climate, the MDV are one of the few places in Antarctica

where liquid water can be found at or near the surface, either in ephemeral summer streams or perennially ice-covered lakes. As is typical of desert climates, many of the lakes have saline bottom waters (Lyons et al., 2005).

The lakes, streams, and climate of the MDV have been studied for decades as part of the National Science Foundation funded Long Term Ecological Research (LTER) program (www.mcmlter.org), which is partly a continuation of monitoring performed by the New Zealand Antarctic Program since the late 1950s. Our knowledge of the subsurface and any associated groundwater is limited to geophysical exploration done in preparation for the Dry Valley Drilling Project (DVDP) (McGinnis and Jensen, 1971; McGinnis *et al.*, 1973) and the subsequent drilling effort (Decker and Bucher, 1977; McGinnis and Osby, 1977; Stuiver *et al.*, 1981; Cartwright and Harris, 1981). Results from these investigations offer ambiguous evidence for subsurface water. Electromagnetic (EM) resistivity and active-source seismic investigations were interpreted as being indicative of liquid brines trapped under relatively thin frozen ground (McGinnis *et al.*, 1973). Based on a few such measurements near lakes, McGinnis *et al.* (1973) postulated that these brines were part of a 'continuous hydrogeological unit' in the region. Thermal measurements from DVDP boreholes indicated that permafrost, broadly defined as any material that is perennially below zero degrees Celsius but not necessarily devoid of liquid brine, was widely present in the MDV to depths up to almost 1000m (Decker and Bucher, 1977) and therefore largely isolated the surface hydrologic features from any groundwater at depth (Cartwright and Harris, 1981). Since then, research on the MDV hydrologic system has focused on the

contributions of water and solute transport in the active layer (Dickson *et al.*, 2013; Levy *et al.*, 2011; Toner and Sletten, 2013; Toner *et al.*, 2013) and surface streams (*e.g.* Lyons *et al.*, 2005). Surface hydrology research has flourished in part due to greater accessibility and the LTER research theme of investigating surface connectivity.

Studies of subsurface hydrology are often complicated by varying uses of the term permafrost. Permafrost is commonly defined as ground that is perennially below 0°C (Ferrians *et al.*, 1969; Cartwright and Harris, 1981; Osterkamp and Jorgenson, 2009), but some authors explicitly define it as frozen ground without liquid water or brine in pore spaces (*e.g.* Minsley *et al.*, 2012). The distinction is important in areas where solute concentrations can significantly depress the freezing point of water, as in the MDV. This paper uses the more common definition of permafrost as sub-zero degree Celsius ground. Previous authors may have associated such permafrost with barriers to groundwater flow, but this is not necessarily the case and this imprecision may have helped discourage investigation of groundwater in the MDV after the early 1970s.

Due to increased environmental protection of the MDV as part of an Antarctic Specially Managed Area (ASMA), permafrost drilling in the future will have to be undertaken sparingly and with due attention to environmental stewardship. Thus, low impact geophysical techniques are necessary to investigate regional subsurface hydrology and its connectivity to surface features and the coastal ocean. First used in the 1970s in the MDV, electrical resistivity methods remain an effective way to

investigate subsurface distribution of brines.

Transient electromagnetic (TEM) methods are known to be highly sensitive to electrically conductive targets such as brine or wet clays, which return strong inductive secondary electromagnetic fields. Resistive geological units like dry sand, ice, or frozen permafrost, give weaker responses, often close to ambient noise levels (Ward and Hohmann, 1988; Christiansen *et al.*, 2006). For this reason, the TEM method and more generally all induction EM methods have been intensively used for the mapping of conductive units. Hydrogeologic and resource applications of TEM include mapping clay-rich aquitards which offer protections for aquifers (Palacky, 1987; Kirsch *et al.*, 2003; Foged *et al.*, 2014), seawater intrusion in coastal aquifers for water quality control and management (Kirkegaard *et al.*, 2011; Teatini *et al.*, 2011; Jørgensen *et al.*, 2012) and mining exploration of highly conductive mineral deposits (Smith, 2014). Recently, Minsley *et al.*, (2012) used frequency domain EM to map permafrost above groundwater in arctic Alaska.

Because the MDV contain high resistivity ice and low resistivity brines, there exists a large EM-resistivity contrast between frozen ground and ground containing liquid brine (Dugan et al., 2015a; Mikucki et al., 2015). This paper presents results from the first airborne electromagnetic (AEM) survey in Antarctica, performed in November, 2011 in select locales in the MDV, and expands on the technical aspects of the AEM system, with comparisons to other techniques and past geophysical exploration. The survey was done using the SkyTEM system developed by the Hydrogeophysics Group at University of Aarhus (Sørensen and Auken, 2004) which

also wrote accompanying data processing algorithms (Auken *et al.*, 2009). AEM combines a large depth of investigation with the mobility and high spatial resolution afforded by helicopter borne equipment (Sørensen and Auken, 2004). This AEM survey provides a regional-scale high-resolution 3D representation of subsurface resistivity in MDV. It significantly expands the understanding of the subsurface geology and hydrology compared to the geophysical measurements made in the early 1970s. Numerous measurements of lake conductivity and the DVDP boreholes in the 1970s allow us to validate our data.

METHODS

Airborne electromagnetic (AEM)

In the MDV survey we used the SkyTEM system initially developed in the early 2000s for hydrogeological mapping (Sørensen and Auken, 2004). It is based on the Time Domain Electromagnetic Method (TDEM) which measures the secondary electromagnetic field induced in the ground after an abrupt turn-off of a pulsed primary electomagnetic field generated by a large transmitter loop several hundred square meters in area. The time decay of this secondary electromagnetic field is generally measured by using an induction receiver coil (a compact solenoid of tens of square meters of effective area) which records the time derivative, or electromotive force, of the magnetic field. This measure is usually denoted as $\frac{\partial b}{\partial t}$ with units of V/m² (the voltage measured between the two extremities of the receiver coil normalized by its area). In

late times, after the primary field has decayed

$$\frac{\partial b}{\partial t} \approx -\frac{I\sigma^{3/2}\mu_0^{3/2}a^2}{20\sqrt{\pi}} t^{-5/2} \quad (1)$$

where I is current, σ is conductivity, μ_0 is the permeability of free space, a is the radius of the coil and t is time (Ward and Hohmann, 1988). Importantly, apparent conductivity can be determined as a function of time, giving a first overlook of the conductivity variations as function of depth. This equation also highlights that measured $\frac{\partial b}{\partial t}$ decreases proportionally to $t^{-5/2}$, which means that the TDEM signal decreases by 5 orders of magnitude per 2 orders of magnitude in time. Usually 2-3 orders of magnitude of time are observed in practice, so an efficient TDEM measurement device needs to be able to record differences of electric potentials that can be 1 billion times different in amplitude (from ~1V down to μV).

Most recorded TDEM responses cover the equivalent frequency range from 10 Hz to about 300 kHz. The high frequency content is used to invert for electrical properties of the near surface at relatively high vertical resolution based on TDEM measurements made immediately after turning off the primary current in the transmitter loop. As time elapses, TDEM measurements provide information on electrical resistivity at increasing depth. These later signals come from the lower frequency part of the spectrum leading to decreasing vertical resolution. There are practical challenges to acquiring both near-surface and deep information due to the longer time required to

shut down the higher primary current in the transmitter loop, which filters the highest frequency content, and due to the decreased signal-to-noise ratio at late times.

Because ground TDEM response globally decreases as a factor of $t^{-5/2}$ and time windows for recording the secondary ground response span from about 10 μs to few ms, there is a huge drop of signal level for a single TDEM sounding. If the moment (the product of current, loop area, and number of wire turns) in the transmitter loop is increased to improve the signal-to-noise ratio for late observation times, the turn-off becomes longer and near-surface vertical resolution deteriorates. To tackle this issue the SkyTEM system transmits current at low (LM) and high (HM) transmitter moments to achieve an improved broadband system. The LM is optimized for near-surface mapping by providing higher frequency content via its faster turn-off, while the HM is optimized for deep investigation by increasing the ground TDEM response above the

noise level at late times via high current and multiple turns (Figure 1a).

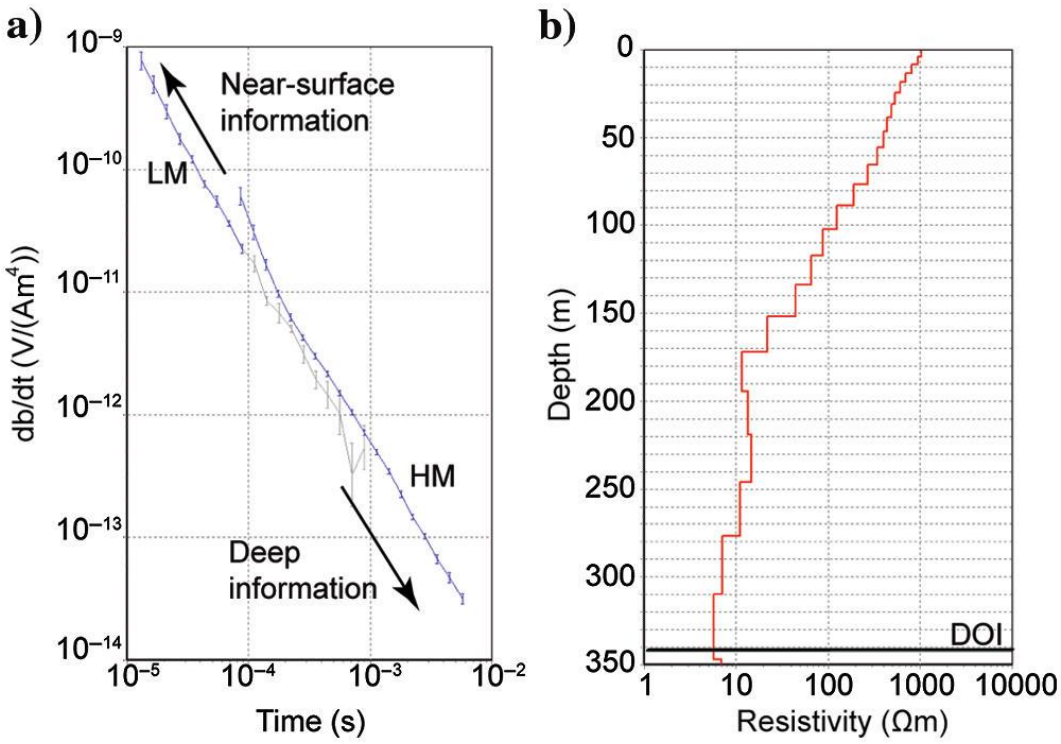

Figure 1.1: (a) typical dual moment transient electromagnetic (TEM) curve with both low (LM) and high (HM) moments (the two curves are normalized by the moment); (b) the corresponding 29-layers resistivity model with its estimated depth of investigation (DOI). The sounding position is indicated on profile shown in Figure 4.

AEM compares favorably to the more commonly used radio echo sounding technique for creating regional-scale geophysical datasets in areas where low resistivity material is widespread. Both techniques utilize time-variable electromagnetic field, but in the EM induction approach the field varies slowly enough for its propagation part to become negligible compared to the diffusion term (i.e., the second order time derivative of the field strength is negligibly small). EM induction frequencies are typically a few to several orders of magnitude lower than radio echo sounding frequencies, resulting in wavelengths much larger than the skin depth of field

penetration (Zhdanov, 2009). The high frequencies used in radar applications mean that the second time derivative of field strength is non-negligible and its propagation is described by the wave equation. Under conditions of low conductivity, radar waves have small wavelengths relative to their skin depths. The skin depth, δ, of an EM field (frequency, f ~< 10^5 Hz) is proportional to $\sqrt{\left(\frac{\rho}{f}\right)}$, so low frequency fields or high resistivity materials lead to large skin depths (Sharma, 1997). For radar (frequency ~> 10^7 Hz), $\delta \propto \rho$; radar therefore is sensitive to changes in dielectric constant and is strongly attenuated in low resistivity materials (Sharma, 1997). Consequently, while the higher frequency radar has higher spatial resolution than EM induction methods, radar waves penetrate less deep into the ground than diffusive EM fields, particularly when conductive materials are present. EM frequency can be tuned to penetrate through some thickness of conductive materials, with more conductive material requiring lower frequency fields (Sharma, 1997).

The SkyTEM504 system flown for our MDV survey has a total weight of approximately 500 kg, a transmitter area of ~500 m², four transmitter coil turns and a current for the HM moment of 95 Amp. The resulting maximum depth of investigation is approximately 350 m depending on the conductivity of the subsurface. The transmitter frame was assembled on the sea ice near the US McMurdo Station. Figure

2a shows the first calibration lifts by the Bell 212 helicopter.

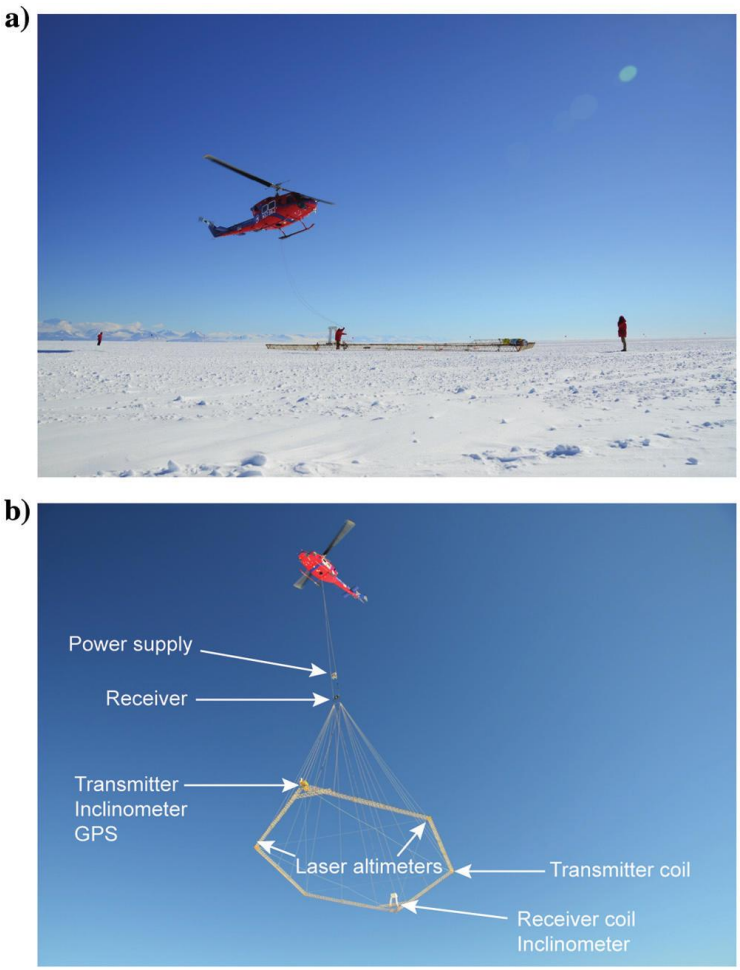

Figure 1.2: (a) The SkyTEM504 frame being lifted by a Bell 212 helicopter on the sea ice outside McMurdo station, 2011; (b) SkyTEM504 system in the air.

Data acquisition

Average flight altitude of the survey was about 35 m above ground surface. Flight lines were spaced by 200-400 m (Figure 3), the average flight speed was 55 km/h and the effective sounding spacing along the lines was about 50 m after averaging 3 raw datasets into one. TEM data used in this study were collected between 13 μs and 8 ms from the beginning of the current turn-off, with the beginning of this time record

corresponding to 8 μs after the end of the transient response ramp. Each sounding corresponds to two consecutive LM and HM pulses linked to one GPS position and constitutes a dual-moment sounding curve (Figure 1b). The LM part of the curve has a stack of 256 transients (each one lasts ~2 ms including the period of injection and the period over which the secondary electromagnetic response is measured), and the HM a has stack of 64 transients (each one lasts ~16 ms). Additional software stacking is carried out during processing in order to improve signal-to-noise ratio at late measurement times. Two lasers mounted on the frame measure its altitude during flight. The frame pitch and roll are recorded using two tilt meters also mounted on the frame. The position of all these devices is indicated in Figure 2b. Data were kept up to a maximum altitude of 70 m above the surface and frame pitch and role rarely exceeded +/- 10°.

Data processing

The main processing steps follow the work of Auken *et al.* (2009) and are described here briefly. Correction to compensate pitch and roll of the loop were done automatically via continuous tilt measurements during the survey. Altitude records from the lasers required no manual corrections, as there is no vegetation on the surface of the MDV.

Prior to the survey the AEM system was calibrated at the national reference site in Denmark to correct the signal amplitude and time shifts (Foged *et al.*, 2013). For the calibration of the system, the estimated time shift is less than -0.7μs for LM, -3 μs for

HM and an amplitude shift factor 0.92. These shifts have little effect on the data but ensure measurements are calibrated to the best possible accuracy.

Two main precautions for the sounding curves were considered:

- Early times at LM (Figure 1a): there was still some residual current in the transmitter loop at the first times recorded just after the turn-off. This system response is called coil response (CR) and is measured with the AEM system flown at high altitude (> 1000 m) where no ground response can be measured. The CR was later removed during data inversions (Schamper *et al.*, 2014). In the MDV, some areas were so resistive within the depth of signal penetration that only CR data were recorded. Correction for the CR effect during data inversion is important to avoid a misleading interpretation of early times (Schamper *et al.*, 2014) resulting in the location of false conductive or resistive layers in the shallow subsurface.
- Late times at LM and HM (Figure 1a): in areas where no conductive layers are present in the subsurface, many late time gates were below the noise level and were removed from the dataset. If noisy late times are kept, it results in fictitious deep conductive layers. In many areas of the MDV only a few gates remained after this cleaning process. When the number of remaining gates was too low (< 4), these data were removed before inversion.

A gate-by-gate plot of a typical section across Lake Fryxell is shown in Figure 4a. The gates for each TEM sounding are shown along the flight line, illustrating the

different levels of signal detected. As shown, 1) both LM and HM have high signal above Lake Fryxell which contains brackish water; 2) just the HM signal is high outside of the lake where there is only a deep conductor (permafrost with brines) with a resistive cover (permafrost with no liquid water in pore spaces) as seen on the northwestern side of the profile (Figure 4a); and 3) on the most northwestern part of the profile the entire signal drops and HM has only a few gates remaining indicating very thick high resistivity permafrost and no conductive layers within the entire range of depth penetration.

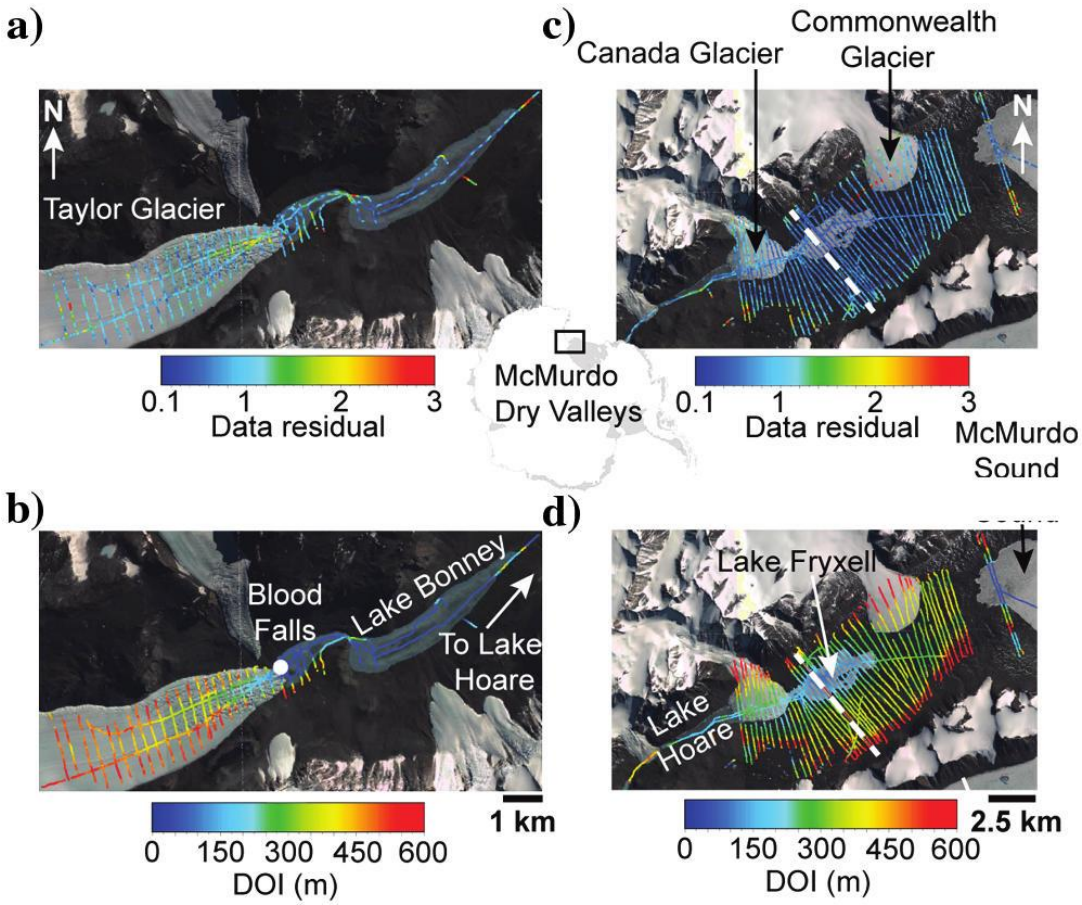

Figure 1.3: Flight lines after data processing with data residual for Taylor Glacier (a) and Taylor Valley (c), and depth of investigation (DOI) for TG (b) and TV (d) as

colored points. The dashed white line corresponds to the profile shown in Figure 4.

To maintain good near-surface resolution and to improve the signal-to-noise ratio at late times, trapezoid filters (which average early times less than late ones) with stacking windows enlarging with time delay were applied. This way there is no additional loss of lateral resolution in the near surface with a narrow stack window (6 s for first gates of MCM survey), and reduction of noise with a wider window at late times for a better depth of investigation (up to 20 s for the latest gates) (Auken *et al*., 2009).

Data inversion

Modeling and inversion of the AEM data was carried out with the AarhusInv program (Auken *et al.*, 2014, Kirkegaard and Auken, 2015) using Aarhus Workbench (www.hgg.au.dk). We used the spatially constrained inversion (SCI) scheme (Viezzoli *et al.*, 2008, Auken and Christiansen, 2004) providing a quasi-3D resistivity model of the ground with local vertical forward and derivatives calculations. Each sounding position corresponds to a local 1D resistivity model, which is linked by spatial constraints to its neighboring soundings. Those constraints ensure continuity between adjacent soundings. For this inversion, lateral constraints were set to a factor of 1.35 and increased rapidly beyond a radius of 20 m. This means resistivity values can vary within 35% from one sounding to another. These constraints are not strict and do not forbid sharp changes if the fitting with the data requires it. Each vertical resistivity model consists of 29 layers with thicknesses starting from 1.5-4 m near the ground

surface and increasing logarithmically until the depth of 350-650 m (Figure 1b), depending on the overall vertical resistivity distribution of each subarea. A many-layered inversion was chosen over a few-layered inversion scheme because the former eliminates the need to make an initial guess on the number of geological layers across the survey area. The change in the number of geological layers is illustrated in Figure 4b: only one overall very conductive layer can be detected above Lake Fryxell whereas varying levels of resistivity within the permafrost can be observed around the lake.

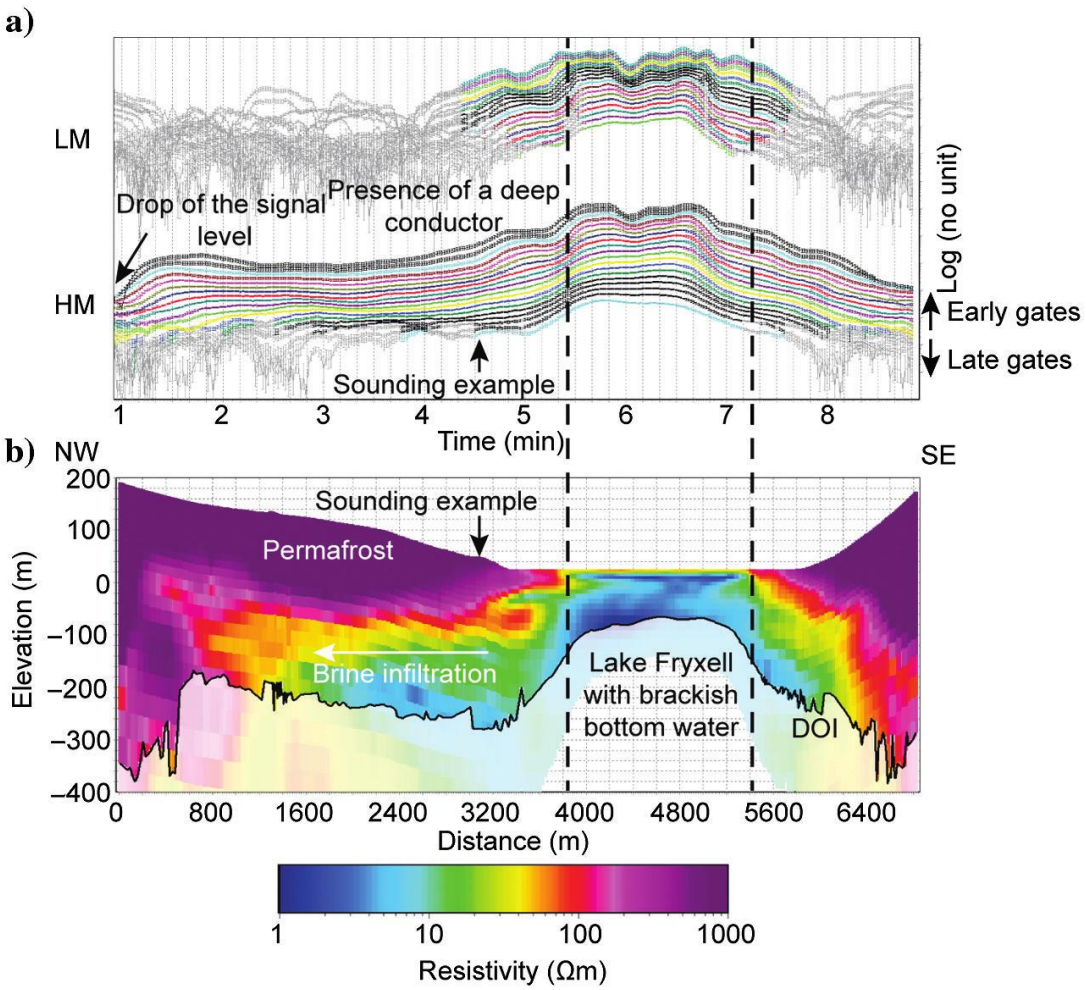

Figure 1.4: Flight line across Fryxell Lake and its surrounding (white dashed line in Figure 3): (a) processed gate by gate data section with low (LM) and high (HM) moments. Too noisy gates are fainted; (b) the corresponding 29-layer resistivity model

section obtained after the inversion. The dark line indicates the depth of investigation (DOI). Location of the sounding example shown in Figure 1 is indicated.

The smooth inversion scheme requires the consideration of vertical constraints between neighboring layers to ensure non-erratic resistivity models. For the MDV dataset the vertical constraints are set loose (factor of 1.6) in order not to overly smooth the sharp transitions (*e.g.* between glacier ice and subglacial brine). Despite this, smoothing in the presented inversion results is still present. It is related to the resolution obtainable with the diffusive induction electromagnetic method. Sharper boundaries can be mathematically obtained (Vignoli *et al.*, 2015), but this must be constrained by other data (*e.g.* radio echo sounding, boreholes) in order to minimize the inherent equivalence issues (where different ground models explain the acquired data equally well). Combining different geophysical data sets with the AEM data to get sharper boundaries is beyond the scope of the present paper, but may be included in future interpretations.

The inversion algorithm uses a forward modeling code in which all parameters of the acquisition device are modeled to avoid misinterpretation of TDEM data (Christiansen *et al.*, 2011): waveform of the current injected in the transmitter loop, low-pass filters of the system, and altitude of the system which is considered as an inversion parameter constrained to the value measured by the laser.

Data and inversion quality control

A number of parameters are checked during quality control of data and inversions. Data processing is quality controlled by checking: 1) the GPS positions,

which need to be consistent with the planned survey and the background GIS map; 2) the continuity of the altitude measurements (20 points every second with laser); 3) any abnormally high tilt values exceeding +/-10°; 4) the presence of too noisy gates (normally fainted as in Figure 4a), which could indicate a non-optimal definition of the noise level (about 5.10^{-8} V/m² at 1 ms for this survey).

The main inversion parameter checked during quality control is the data-fit residual which is the difference between the model output and the field data, normalized by the standard deviation of the data. A data-fit residual below 1 indicates a good fit of the estimated resistivity model into the field data within the observational error estimated using the trapezoidal stack window. An abnormally high residual can have several causes: the noise cleaning process was not sufficient, spatial constraints were too strong to allow resistivities to change enough during the iterative inversion, and/or considered system parameters are badly defined. The overall data residual of an explored area should have its value below one. In the case of the MDV survey, the data residuals are low where brine is present (Lake Bonney in Figure 3a and Lake Fryxell in Figure 3c), and become more erratic where the signal is close to the noise level above resistive areas such as thick brine-free permafrost or shallow bedrock (sides of Taylor Valley in Figure 3c) or glacial ice of more than several hundred meters in thickness (*e.g.*, upstream on Taylor Glacier in Figure 3a). Overall the data residual for the study area is below 1.0. A histogram of residuals for Taylor Glacier (Figure 5a) shows a globally larger data residual than in our Taylor Valley data (Figure 5b), though most of it remains below 1.5. This is due to the large areas covered by thick, high resistivity ice

of Taylor Glacier, which results in a weak secondary EM response. This observation is also illustrated with the statistics in Table 1.

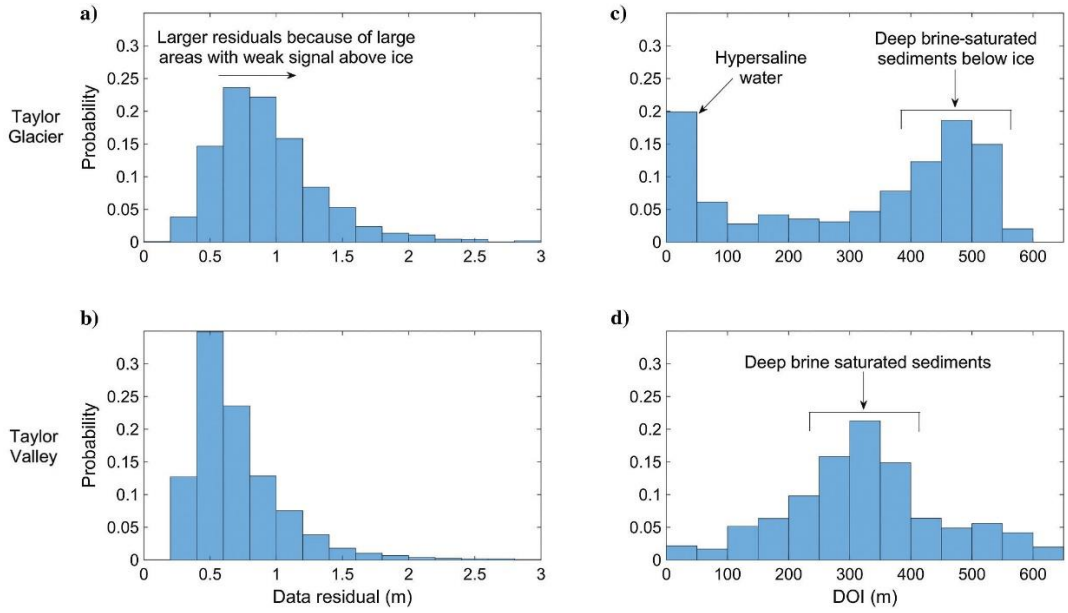

Figure 1.5: Histograms of DOI and data residuals for Taylor Glacier and Taylor Valley

The estimated resistivity models are automatically analyzed at the end of the inversion to evaluate the depth of investigation (DOI) (Christiansen and Auken, 2012). This sensitivity analysis considers the cumulated response of the data to each layer's resistivity from the deepest layer:

$$S_j = \sum_{j=M,-1}^{k} \frac{\sum_{i=1}^{N} \frac{G_{ij}}{\Delta d_i}}{t_j} \quad (2)$$

Where S_j is the cumulated sensitivity from the deepest layer to layer j, M the total number of layers, N the total number of data points, t_j the thickness of layer j, $G_{ij} =$

$\frac{\partial \log(d_i)}{\partial \log(\rho_j)}$ the sensitivity of data point i to the resistivity of layer j, and Δd_i the standard deviation of data point d_i. The total number of layers M can be larger than the number of layers of the inverted model (resistivity is repeated within each inverted layer), in order to get a finer estimation of the DOI. Once the cumulated sensitivity S_j reaches a threshold value which is fixed based on the experience with field data and cross comparisons of models obtained from different methods (Christiansen and Auken (2012) estimate a threshold value within the range 0.6-1.2), the DOI is reached.

This sensitivity analysis provides the basis for fading of the resistivity sections below a depth from which resistivity values have almost no impact on the measurements (*cf.* sounding example of Figure 1b). DOI estimation is important to avoid over-interpretation of deep conductors whose presence may be entirely due the numerical optimization or noisy data inadvertently left in the late part of the TDEM signal. In the present survey the DOI is less than 50 m above brackish to hypersaline lakes (Lake Bonney in Figure 3b and Lake Fryxell in Figure 3d), and reaches about 350-400 m where good conductors are located below high resistivity layers and there is still representative and reliable signal. Where few gates remain with poor signal, indicating that only highly resistive formations (above 1000 Ωm) are present, the DOI estimation can go beyond 400 m (top of Taylor Glacier in Figure 3b, sides of Taylor Valley in Figure 3d). A histogram of DOI values for Taylor Glacier shows a large portion of values smaller than 50 m (Figure 5c). This is due to the presence of hypersaline water close to the snout of the glacier. A large portion of DOI values for Taylor Glacier are also greater than 400 m, likely due to the presence of a deep

subglacial conductor beneath high resistivity glacial ice. Figure 5d also shows DOI values in Taylor Valley are not as high as in Taylor Glacier, with 350 m being the most common. Numerical statistics are available in Table 1.

Table 1.1 Statistics on DOI estimation and data residuals for TG and TV

	DOI TG (m)	Data residual TG	DOI TV (m)	Data residual TV
Minimum	31.9	0.14	29.8	0.11
Maximum	597	12.7	650	13.0
Mean	315	0.97	328	0.74
STD	187	0.57	130	0.55
Median	384	0.87	325	0.62
% < 1	—	63.7	—	83.6
% <1.2	—	79.4	—	91.1
% <1.5	—	90.6	—	96.0
% < 50 m	19.9	—	2.15	—
% >300 m	60.4	—	59.4	—

RESULTS

We collected data from approximately 300 km² of the MDV, with the best coverage over eastern Taylor Valley (Figure 3a,b) and the lower 4 km of Taylor Glacier in western Taylor Valley (Figure 3c,d). This is the most complete regional scale subsurface geophysical dataset of any type collected in the MDV. Its wide coverage and deep DOI allow us to expand upon work done at smaller scales by previous

researchers and complement work done with different geophysical techniques.

Prior to our survey some of the most complete subsurface geophysics in the MDV came from limited measurements from the 1970s. McGinnis *et al.* (1973) used active seismic refraction in conjunction with Schlumberger and Wenner DC resistivity arrays to investigate the subsurface in small areas near potential DVDP borehole sites. At the west end of Lake Fryxell, near the eventual site of DVDP borehole number 7, they measured a transect across a narrow part of the lake using two seismic stations and six resistivity stations. From the data they generated a model (Figure 6a) which presents their seismic and geoelectric interpretations down to about 40 m below the surface. Their models indicate that there are widespread deep areas of relatively lower resistivity (<400 Ωm) covered by high resistivity (1000s to 10,000s of Ωm) material on either shore. They interpreted this situation as sand and gravel saturated with unfrozen water beneath frozen permafrost, which they speculated could be connected to a regional aquifer beneath frozen permafrost.

In the Fryxell Basin, our data produced a model that is consistent with their inferences but much more detailed and in three dimensions. The AEM system is able to constrain resistivity at much greater depths than the techniques used by McGinnis and others; at Lake Fryxell it measures more than 200 m below their deepest measurements. Our regional-scale measurements produce reasonable results: we detect low resistivity material (<100 Ωm) at the lake where there is brackish water, surrounded by with higher resistivity material (100s to 1000s of Ωm) on the shores where frozen ground is expected (Figure 6b). As did McGinnis *et al.* (1973), we measure the highest

resistivities north of the lake. Our data show that the low resistivity area extends laterally underneath the shallow frozen permafrost for 100s to 1000s of meters, representing a large fraction of the valley's width, and down at least 200 m without indication of any clear increase in resistivity until the survey reaches the DOI limit.

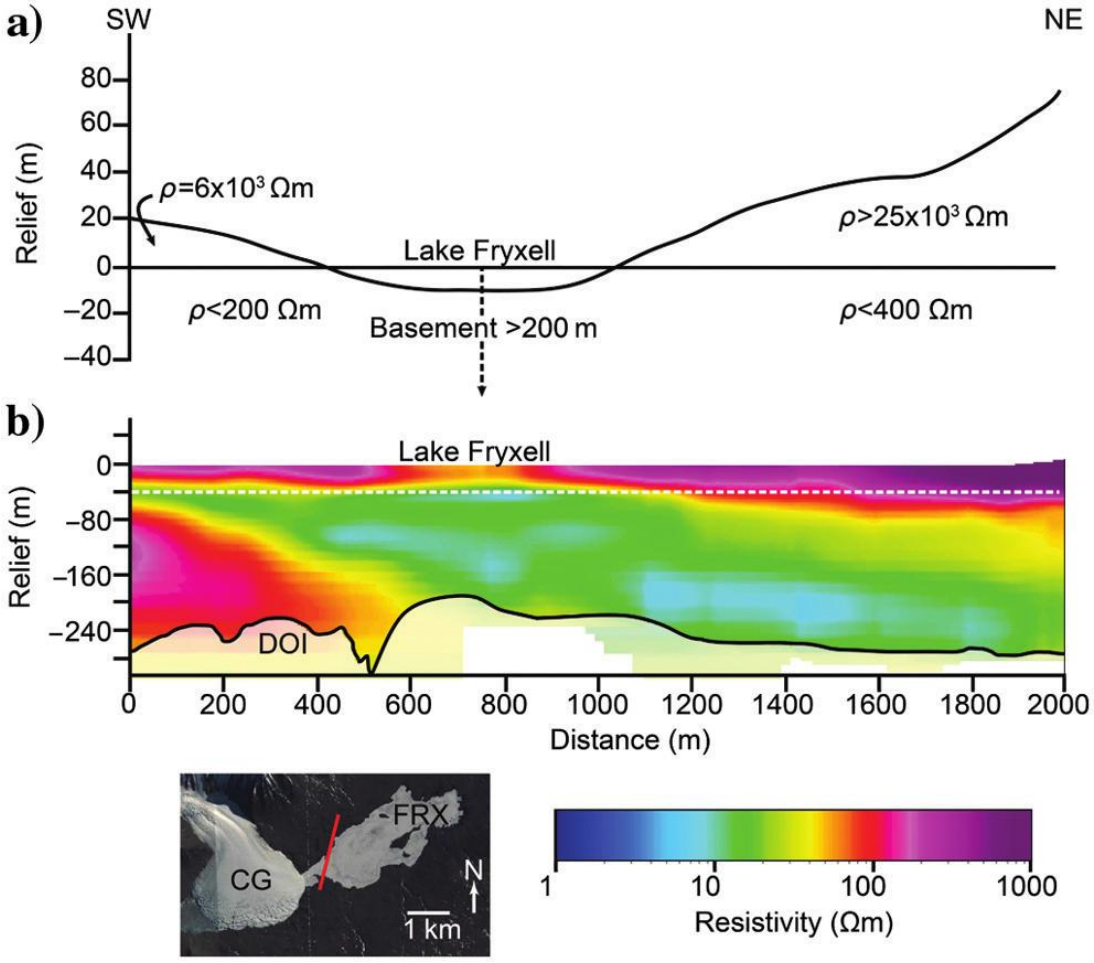

Figure 1.6: Profile across Lake Fryxell: (a) simplified version of McGinnis et al. (1973) model; (b) our model, with the maximum depth of the 1973 model marked by the dashed white line. Inset: Map of area; CG=Canada Glacier, FRX= Lake Fryxell, red line marks profile.

Unfortunately, the DVDP borehole drilled in the Fryxell Basin, DVDP 7, penetrated, with difficulty, a mere 11.2 m before the borehole collapsed (McGinnis and

Osby, 1977) and consequently yielded little information, so it is not very useful for comparison to our measurements. Further east, DVDP 11 near Commonwealth Glacier achieved a depth of ~310 m, at which point it lost drilling fluid (McGinnis et al., 1982), potentially indicating a permeable aquifer. An AEM sounding at the same location shows a sharp drop in resistivity between depths of 200 and 275 m coincident with sharp increases in salinity within marine sediments (Figure 7). This occurs over a range of temperatures (~-10°C to -6°C) consistent with temperatures at which MDV brines could exist: the saline bottom waters of Lake Bonney are -5.3°C (Spigel and Priscu, 1996); water exits Blood Falls, a hypersaline discharge at the terminus of Taylor Glacier, at -5.6°C (Mikucki *et al*., 2009); and Hubbard *et al.*, (2004) predict basal temperatures beneath Taylor Glacier, where brine is present, to be at most -7.8°C Further east DVDP 10 filled with 72 ppt brine at about 180m deep (McGinnis et al., 1982) and circa -6° C (Decker and Bucher, 1982), indicating that there can be at least

localized areas of hypersaline brines at depth within permeable sediments.

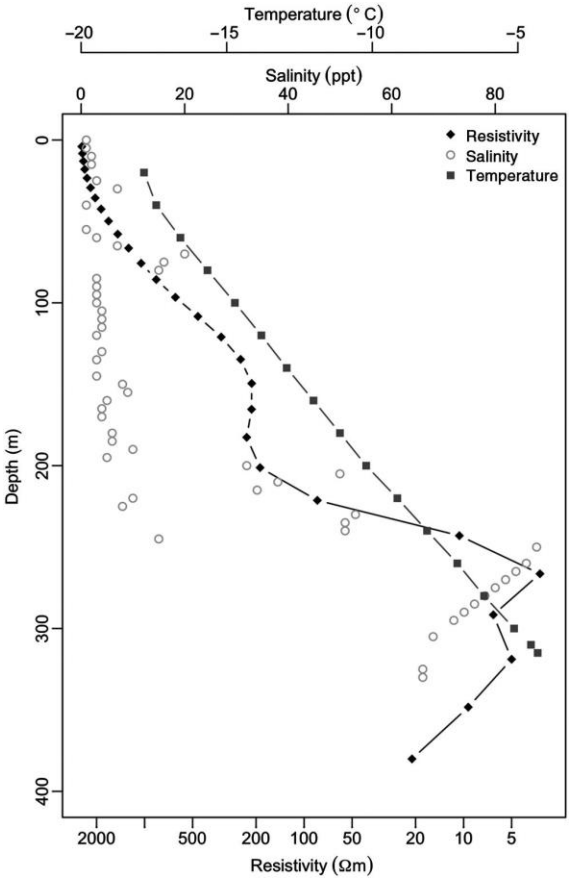

Figure 1.7: AEM data compared to DVDP 11 borehole temperatures (Decker and Bucher 1982) and salinity (McGinnis et al. 1982). DVDP 11 borehole location is marked in Figure 8.

Regional Cross Section

A regional scale view shows that the deeper layer of low resistivity measured in cross section at Lake Fryxell (Figure 6b) is representative of the eastern portion of Taylor Valley. At an elevation of -150 m, low resistivity material is widespread throughout the lower reaches of the valley from Canada Glacier to the Ross Sea (Figure

8). The maximum depth of Lake Fryxell is ~20m, therefore resistivities at -150m are well within sediments and bedrock beneath the lake bottom. The extent of this low resistivity zone far exceeds the shores of Lake Fryxell, indicating that this represents a region of liquid groundwater that is outside the thermal influence of Lake Fryxell's talik, and therefore a truly regional aquifer. About half of the measurements taken in eastern Taylor Valley at all depths have resistivities 100 Ωm or less, suggesting widespread brines. This potential aquifer may connect at depth with the Ross Sea, particularly in two 'channels' of low resistivity material that are visible on the North and South edges of Coral Ridge (Figure 8), an otherwise high resistivity moraine complex from the last glacial maximum expansion of the Ross Ice Shelf (Hall et al.,

2000) that separates Taylor Valley from the Ross Sea.

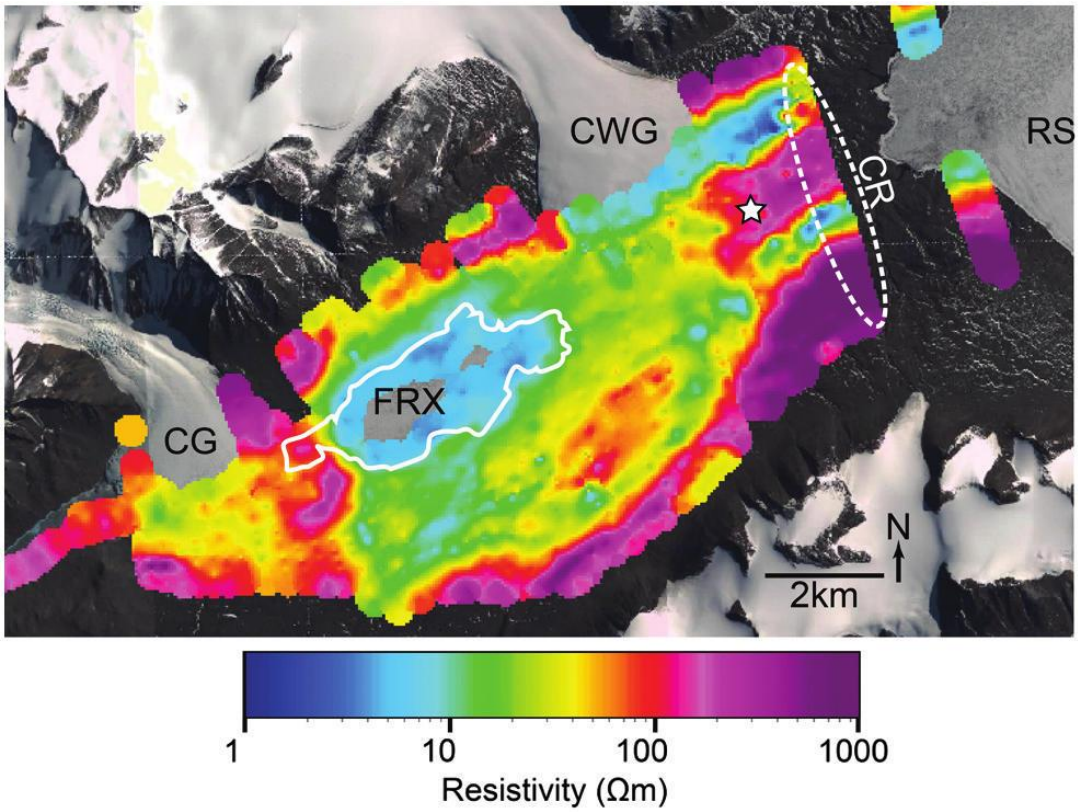

Figure 1.8: Resistivity at -150m elevation. Solid white line indicates the surface expression of Lake Fryxell (FRX), dashed white ellipse marks general location of Coral Ridge (CR). Star marks the location of DVDP 11. CG = Canada Glacier, CWG = Commonwealth Glacier, RS = Ross Sea. No data in central Lake Fryxell because this is below the DOI at this location.

Radio Echo Sounding and AEM

Radio Echo Sounding (RES) has been used infrequently in the MDV. Due to the labor involved with operating a ground-based unit, RES has typically been used to investigate small-scale features in the MDV like possible delta deposits and moraines (Arcone *et al.*, 2000; Arcone, 2002), dunes (Bristow *et al.*, 2010), lake ice (Dugan *et al.* 2015b), or glacial accumulation zones (Arcone and Kreutz, 2009; Shean and

Marchant, 2010; McKay *et al*., 2014). We are aware of only one regional scale airborne RES investigation (Holt *et al.*, 2006), which was used primarily as a calibration exercise for potential future use of RES on Mars.

Compared to most RES measurements made in the MDV, AEM observes a far deeper domain. For example, Arcone et al. (2000) used 100 MHz radar at central Coral Ridge, to trace slightly dipping reflectors to a depth of 23m, with implications for the emplacement history of the drift. At the same location on Coral Ridge, our AEM survey was able to measure up to 300m below the surface. It detected large areas of low resistivity at depth beneath extremely high resistivity material in the center of Coral Ridge, potentially stranded ice (Figure 9). There is a gap in the AEM data coverage between Coral Ridge and the Ross Sea, but the available data are suggestive of a deep connection between the Ross Sea and Taylor Valley beneath Coral Ridge (Figures 8

and 9); this feature was not detected in radar or DVDP borehole logs (Powell, 1981).

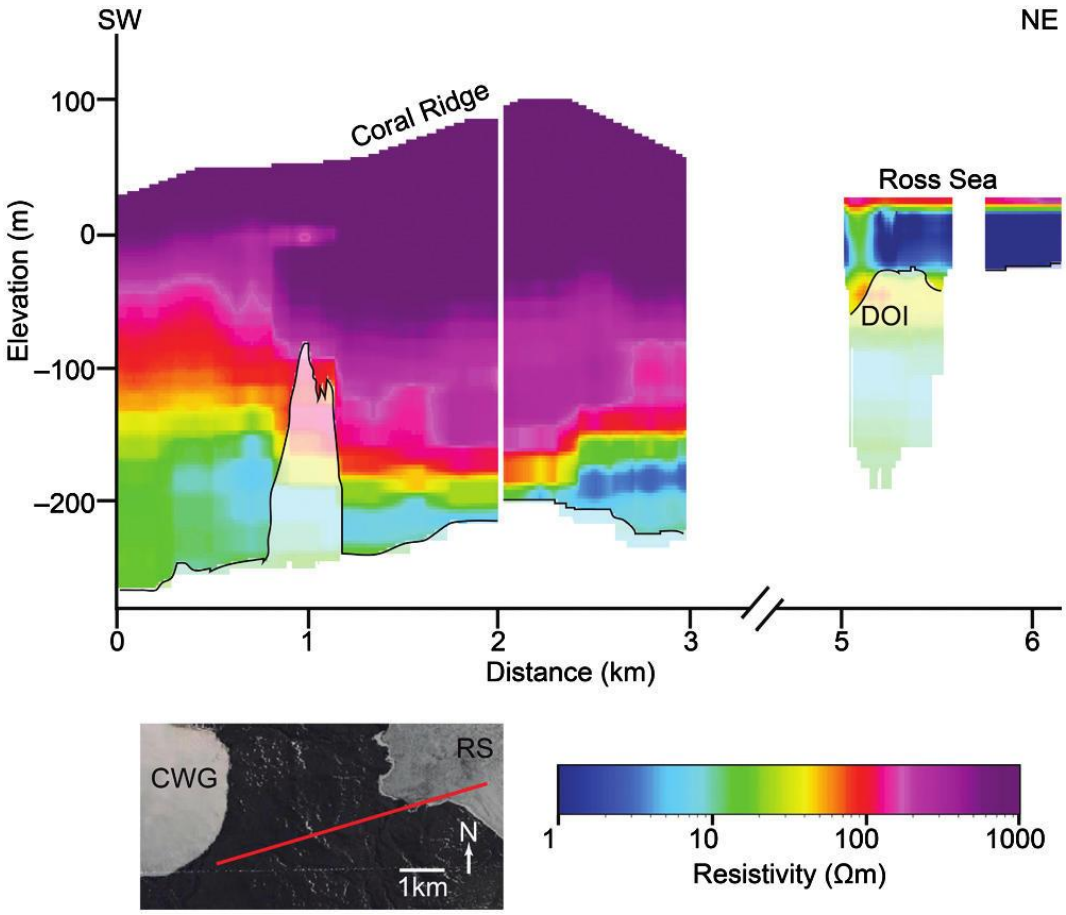

Figure 1.9: Resistivity Profile across Coral Ridge. X-axis (distance) shortened over section of missing data. Inset: Map of area. CWG=Commonwealth Glacier, RS=Ross Sea.

Low frequency radar (10–100 MHz) is commonly used to measure basal topography of glaciers (*e.g.* Berthling *et al.*, 2000; Isaksen *et al.*, 2000; Degenhardt and Giardino, 2003; Hubbard *et al.*, 2004; Engel *et al.*, 2012), while shorter wavelength (100-400 MHz) is used when high resolution is required (*e.g.* Fukui *et al.* 2008; Sold *et al.* 2014). As the speed of electromagnetic waves in ice is in the range of 0.167-

0.169 $m.ns^{-1}$, which adds some uncertainties depending on the value chosen), the vertical resolution (about quarter of the radar wavelength) ranges from ~4 m at 10 MHz to 0.1 m at 400 MHz. Hubbard *et al.* (2004) used 10 MHz radar to image the lower part of Taylor Glacier, which terminates in Lake Bonney at the western end of Taylor Valley. Based on strong basal reflectivity, they inferred the presence of a liquid water reservoir stored in an overdeepening located three to six kilometers from the glacier terminus. Thermal modeling indicated that the bed was everywhere below the pressure melting point of fresh water, leading Hubbard *et al.* (2004) to conclude that to remain liquid such water must be hypersaline brine. Since AEM is sensitive to subsurface fluid salinity and can cross thicker layers of brine than radar by virtue of larger skin depth, it offers a natural complement to radar for testing the scenario proposed by Hubbard and colleagues (2004). AEM's ability to measure through greater thickness of brine allows for more quantitative estimates of volume and salinity. We detect a horizontally continuous unit of low resistivity material beneath the center of Taylor Glacier which is present from its terminus in Lake Bonney until it is masked by the DOI 5-6 km up glacier (Figure 10). In the up glacier reaches of our profile, AEM cannot penetrate through as much ice as the radar used by Hubbard *et al.* (2004) (~300 m with AEM vs. ~450 m for GPR), but we do see spatial patterns of resistivity consistent with an overdeepening filled with low resistivity material that is distinguishable from the extremely high resistivity glacier ice. Based on this low resistivity, it has been interpreted as hypersaline brine (Mikucki et al. 2015), which is consistent with the high salinity measured in Blood Falls (Keys, 1979; Lyons *et al.* 2005; Mikucki *et al.* 2009),

a hypersaline surface discharge at the terminus of Taylor glacier (Figure 3b), and with the hypersaline bottom waters of Lake Bonney (Spigel and Priscu, 1996). A greater DOI from a higher moment transmitter would allow investigation farther up Taylor Glacier and constrain the size of this subglacial reservoir. Based on the presently available data, it is estimated that the volume of subglacial brine-saturated sediments is at least 1.5km^3, which assuming a conservative estimate of the porosity at 12%, represents a volume of liquid water equivalent to the combined volume of the largest Taylor Valley lakes (Mikucki *et al.*, 2015).

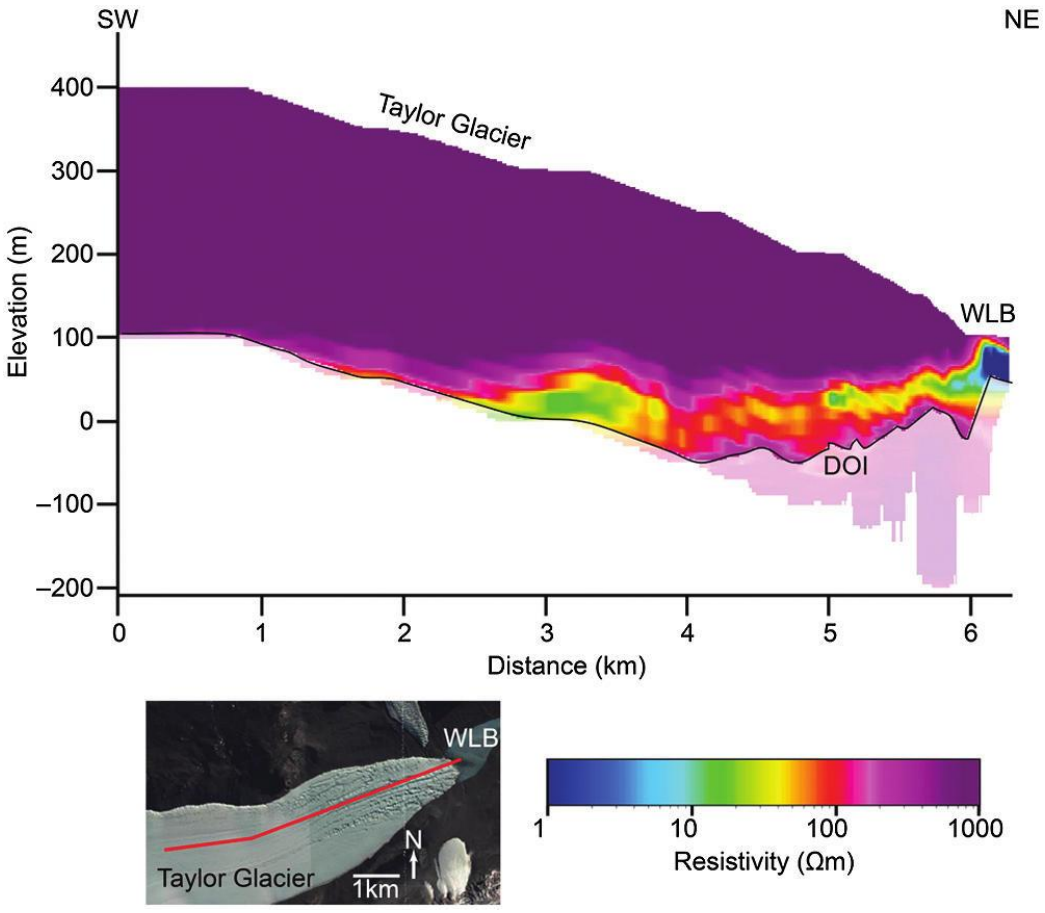

Figure 1.10: Profile along length of Taylor Glacier. Inset: Map of area. WLB=West

Lake Bonney. Blood Falls is at the terminus of Taylor Glacier in WLB.

DISCUSSION

This mapping of permafrost, glaciers, and subsurface liquid brine using AEM in the McMurdo Dry Valleys demonstrates the potential applicability of this technique for future investigations in Antarctica and the Arctic, where regional-scale geophysical datasets will have impacts across disciplines. The effects of climate change and resultant feedbacks are predicted to be the most extreme at high latitudes (IPCC, 2007). Changes in surface and near-surface polar environments may trigger climate feedbacks, such as methane release from warming permafrost (Zimov *et al.*, 2006; McGuire *et al.*, 2009; Paytan *et al.*, 2015) and from beneath retreating ice sheets (Wadham *et al.*, 2008; 2012). Polar ice sheets may become important contributors to global sea level rise as the climate warms (*e.g.*, Joughin *et al.*, 2012).

Subsurface liquid water in particular plays an outsized role in high polar environments. Liquid water beneath glaciers and ice sheets is an important factor controlling glacier motion (Winberry *et al.*, 2011; Creyts and Schoof, 2009; Kamb, 1987). However, Taylor Glacier is considered to be a cold-bottomed glacier whose movement can be explained entirely by internal deformation (Kavanaugh and Cuffey, 2009; Petit *et al.*, 2014). The widespread low resistivity area detected beneath Taylor Glacier, which is consistent with hypersaline brine, may require this model to be reevaluated in light of unexpectedly abundant basal fluids. Other coastal glaciers in

Antarctica may similarly have saline brines lubricating their bases or modifying the rheological properties of their basal ice, which would otherwise be too cold to contain liquid fresh water.

Antarctic subsurface liquid water has been shown to provide a viable habitat for microbes in an environment that is otherwise inhospitable (*e.g.*, Christner *et al.* 2014). Antarctic briny aquifers may provide the best terrestrial analogues for potential subsurface habitats on Mars (Gilichinsky *et al.*, 2003, 2007; Mikucki *et al.* 2015). Ancient water exiting from beneath Taylor Glacier at Blood Falls contains an assemblage of microbes using metabolic pathways enabling them to survive in an environment that may be analogous to a Snowball Earth refugium (Mikucki and Priscu 2007, Mikucki *et al.*, 2009) and conditions beneath frozen permafrost in the MDV may be similar. Groundwater may transport nutrients throughout the subsurface, providing important limiting nutrients such as iron to the coastal ocean (Wadham *et al.*, 2013; Mikucki *et al.* 2015)

In a matter of days, the AEM system increased our understanding of subsurface water in the MDV more than the decades of prior geophysical surveying and borehole investigations. Our results are broadly consistent with past geophysical investigation but because our data cover a larger area and penetrate deeper into the surface, they yield a more comprehensive regional picture of subsurface conditions. We interpret the areas of low resistivity underneath Taylor Glacier and eastern Taylor Valley as a large reservoir of liquid hypersaline brine stored within sediments. Unlike previous methods, we covered enough of Taylor Valley to demonstrate the continuity of this brine over

large parts of the valley, including likely hydrologic connectivity to the lakes through taliks and to the ocean beneath Coral Ridge. Geochemical studies of MDV lakes conducted over the last several decades have tended to discount the importance of deep groundwater flow into and out of the lakes (*e.g.* Lyons *et al.*, 2005; Poreda *et al.*, 2004) but the presence of such a large subsurface brine reservoir should motivate re-evaluation of this assumption. The origin of the salts in MDV lakes is complex and believed to be variable for each lake (Lyons *et al.*, 2005), but the brines beneath the surface may be more likely to share a common heritage. In the northern hemisphere, cryogenic processes have been invoked to explain the presence of shield brines (Herut *et al.*, 1990; Starinsky and Katz, 2003). In the MDV, cryogenic processes may continue to occur in the subsurface, as permafrost freezes in response to the draining of Lake Washburn or as saline waters exit Taylor Glacier from an overdeepening through colder near-surface ice. The DOI of the AEM device is well suited to the scale that continuing freezing may occur over. A Stefan Condition estimate (depth of freezing, $z \approx D\sqrt{t}$ where D is a constant between 1 and 5 that reflects the thermal properties of permafrost, after Osterkamp and Burn (2003)) suggests that permafrost growth since the draining of Lake Washburn around the LGM (Hendy, 2000) should range from roughly 100-500m. This is consistent with our measurements in Lower Taylor Valley showing markedly decreased resistivity ~150-250 m below the surface.

Based on resistivity recorded at the site of DVDP 11, liquid brines in Taylor Valley could exist at temperatures as cold as -10°C (Figure 7). While ground at this temperature fulfills the definition of permafrost, it is not a hydrologic barrier equivalent

to frozen permafrost. Indeed, it could contain a large fraction of pore space filled with water. Archie's Law (Archie, 1950), an empirically determined relationship between bulk resistivity and porosity, can be used to estimate porosities in brine-saturated sediments. A simplified form is:

$$\varphi = \left(\frac{\rho_0}{\rho_b}\right)^{-1/m} \quad (3)$$

where φ is the liquid brine fraction, ρ_0 is the bulk measured resistivity of the formation, ρ_b is the resistivity of the brine, and m is a cementation exponent that reflects properties of the pore network and typically ranges from 1.4 to 2.8. Because the resistivity of the brine is not known and a cementation exponent for permafrost has not been determined, we calculated a range of possible porosities given reasonable values (Table 2). Based on moderate values (ρ_b equal to water at the hypersaline bottom of West Lake Bonney and m=2, a value often used for sandstone) a measured resistivity of 10 Ωm (7% of measurements) could have an unfrozen brine fraction of 14.5%.

AEM has significant potential for further scientific investigations in coastal environments of Antarctica and the Arctic. Polar environments, where water commonly exists as a solid near the surface but can be liquid at depth, exhibit a range of resistivities that spans several orders of magnitude, making geophysical identification easy. Brines enhance this effect, but resistivity has been used to similar effect in freshwater systems in the Arctic (Minsley *et al.*, 2012). The MDV, as a system with brines beneath frozen ground and glacier ice, are potentially not unique in Antarctica, at least not in the

subsurface. Parts of coastal Antarctica could have been flooded by seawater in the past, particularly with continental crust being depressed by weight of glaciers (after Starinsky and Katz, 2003). The MDV are well explored due to the exposure of solid ground and proximity to McMurdo Station, a logistical hub for the United States Antarctic Program, but other areas farther afield and presently covered by glaciers could have similar widespread brines and may become targets for future AEM exploration. Understanding the hydrogeology of these coastal margins may be

important for evaluating the impact of future climate warming on coastal Antarctica.

Table 1.2 Porosities calculated from resistivities for various possible scenarios.

Porosities Determined from Resisitivity (%)

formation factor m = 1.5		ρ_b (Ωm) Seawater (–1.9 °C) 0.36	Bottom WLB 0.21	Vida Brine 0.15
ρ_0 (Ωm)	1	50.6	35.3	28.2
	10	10.9	7.6	6.1
	100	2.3	1.6	1.3

formation factor m = 2.0		ρ_b (Ωm) Seawater (–1.9 °C) 0.36	Bottom WLB 0.21	Vida Brine 0.15
ρ_0 (Ωm)	1	60.0	45.8	38.7
	10	19.0	14.5	12.2
	100	6.0	4.6	3.9

formation factor m = 2.5		ρ_b (Ωm) Seawater (–1.9 °C) 0.36	Bottom WLB 0.21	Vida Brine 0.15
ρ_0 (Ωm)	1	66.5	53.6	46.8
	10	26.5	21.3	18.6
	100	10.5	8.5	7.4

CONCLUSIONS

Using a helicopter-borne, time-domain electromagnetic sensor, we have quickly filled in major gaps in our understanding of subsurface geophysics in the

McMurdo Dry Valleys. Previous geophysical work in the area, much of it over 40 years old, was performed at a few select localities, and the results were generalized to the whole region with no independent verification elsewhere. Our survey samples the MDV, particularly Taylor Valley, at an unprecedented spatial scale relevant to a range of hydrological, glaciological, and geomorphic processes dominating this landscape. Datasets obtained by the localized past geophysical and borehole investigations serve as ground-truths for our more regional AEM results. We find widespread areas of low resistivity material at depth, indicating cryoconcentrated brines existing at sub-zero temperatures beneath unexpectedly thin frozen permafrost. The contiguous nature of these low resistivity areas at depth and their connection with lakes on the surface suggests the presence of a regional-scale briny groundwater system. Such system may function as an important pathway for long-term transport of chemicals in this slowly evolving landscape. It may also be capable of supporting microbial life, thereby greatly expanding the habitable zone in this high polar desert. On the upstream end of Taylor Valley, our technique demonstrates that the subsurface hydrological connectivity extends directly from West Lake Bonney to the subglacial materials beneath Taylor Glacier at least as far upstream as the AEM system can penetrate the increasingly thick glacier ice. These two observations may require that researchers studying biogeochemistry of MDV lakes take into account the possibility of chemical fluxes between the groundwater system and lakes.

TEM surveys complement other geophysical techniques, especially radar. High frequency radar is used for examining internal structure of near-surface features and

low frequency radar can penetrate deep, especially in polar glacier ice. However, radar signal attenuates quickly in the presence of conductive fluids. Resistivity techniques can make measurements through liquid water, and in the case of brines, which are a common form of liquid water in the MDV, resistivity techniques can return information relevant to subsurface salinity and porosity. Extremely low resistivity brines limit the DOI of EM resistivity techniques and thick ice cover can prevent the imaging of very deep brines, but this can be overcome by using higher moment systems. Advances in EM resistivity techniques will make it even more useful in the MDV and for exploration in similar settings in Antarctica and the Arctic. Due to the important similarities between the MDV and Mars, Antarctica is also a promising location where scientists can improve approaches towards studying subsurface brine systems on other planetary bodies.

Chapter 2: Evidence for Pathways of Concentrated Submarine Groundwater Discharge in East Antarctica from Helicopter-Borne Electrical Resistivity Measurements

ABSTRACT

The Southern Ocean receives limited liquid surface water input from the Antarctic continent. It has been speculated, however, that significant liquid water may flow from beneath the Antarctic Ice Sheet, and that this subglacial flow carries that water along with dissolved nutrients to the coast. The delivery of solutes, particularly limiting nutrients like bioavailable iron, to the Southern Ocean may contribute to ecosystem processes including primary productivity. Using a helicopter-borne time domain electromagnetic survey along the coastal margins of the McMurdo Dry Valleys region of Southern Victoria Land, Antarctica, we detected subsurface connections between inland lakes, aquifers, and subglacial waters. These waters, which appear as electrically conductive anomalies, are saline and may contain high concentrations of biologically important ions, including iron and silica. Local hydraulic gradients may drive these waters to the coast, where we postulate they emerge as submarine

groundwater discharge. This high latitude groundwater system, imaged regionally in the McMurdo Dry Valleys, may be representative of a broader system of Antarctic submarine groundwater discharge that fertilizes the Southern Ocean. In total, it has the potential to deliver tens of gigagrams of bioavailable Fe and Si to the coastal zone.

INTRODUCTION

Submarine Groundwater Discharge (SGD) is broadly defined as the flow of water from the seafloor to the ocean, regardless of its origin as terrestrial or marine water, or a mixture thereof (Burnett et al., 2003). It is increasingly apparent that SGD is a process of significant ecological importance in the world's oceans, as a major transport mechanism for both nutrients and contaminants (Simmons, 1992; Moore, 2009). SGD is generated through three main pathways (Burnett et al., 2003):

(1) Terrestrial hydraulic gradients, which drive Darcian flow;

(2) Oceanic processes, which include wave and tidal pumping, among many others;

(3) Endogenic drivers, which include buoyant instabilities and osmotic pressure.

Of these, only terrestrial hydraulic gradients result in a net flow of groundwater from continents into the ocean; whereas the others recirculate and mix seawater with meteoric water [4]. Santos and others (Santos et al., 2012) also identify processes, such as sediment compaction and bioturbation, that could loosely be considered 'endogenic drivers'.

While quantitative estimates of SGD flux now exist for the global ocean between 70N and 60S (Kwon et al., 2014) observations at high latitudes remain very limited (Lecher, 2017). In the North, for example around the coast of Alaska, observed SGD is driven primarily by tidal pumping in areas with large tidal ranges and permafrost melting elsewhere where tidal effects are limited (Lecher et al., 2016a). Models have been used to simulate the effects of SGD on submarine permafrost and gas hydrates in the Beaufort Sea (Frederick and Buffett, 2015) and evidence exists for ice sheet derived SGD around Greenland during the Pleistocene (DeFoor et al., 2011). By contrast, in the Antarctic, there has been only one direct measurement of true SGD, at Lutzow-Holm Bay in East Antarctica, where abnormally high seepage velocities (10^{-8}–10^{-6} m/s) were observed at a range of ocean depths, many exceeding 100 m (Uemura et al., 2011). This flow is apparently independent of tidal pumping and instead appears to be driven by a high surface gradient in the nearby glacier (Uemura et al., 2011).

Given the longer-term water–rock interactions experienced by groundwaters in high latitude regions, Antarctic SGD has the potential to transport a high load of solutes. For example, SGD at certain sites in Alaska, has been shown to transport more nitrate and silicate than rivers (Lecher et al., 2016a) and has also been shown to transport permafrost derived methane to the ocean (Lecher et al., 2016b). As primary production in most of the world's oceans is nitrate and phosphate-limited (Mahowald et al., 2005), nutrient contributions from SGD can be important ecological drivers on a global scale. Indeed, SGD of natural and fertilizer-derived nitrate and phosphate adds to the large flux supplied by rivers (Slomp and Van Cappellen, 2004).

The Southern Ocean is rich in nitrate and other nutrients, and is the most 'high nutrient, low chlorophyll' (HNLC) region on Earth (Tréguer and Jacques, 1992; Moore and Abbott, 2000). However, iron is notably depleted which limits photosynthetic ocean productivity (de Baar et al., 1990). The low iron is in part due to the thick ice sheet limiting inputs of near-shore terrestrially derived iron as well as a relatively low input rate through atmospheric dust and rivers, which are the primary sources of bioavailable iron to the ocean at lower latitudes (Martin et al., 1990; Gerringa et al., 2012). Instead, the melting of sea ice and marine terminating glaciers may be at least a locally important source of soluble (and bioavailable) iron in the Southern Ocean (Gerringa et al., 2012; Thuróczy et al., 2012). Icebergs may help transport bioavailable iron away from the coast to the open ocean (Raiswell et al., 2008). Wadham and others (Wadham et al., 2013) speculated that runoff from beneath the Antarctic Ice Sheet is capable of exporting a substantial dissolved nutrient load, including reduced iron at fluxes potentially comparable to aeolian deposition and transport by ice rafted debris. Few subglacial waters in Antarctica have been directly sampled, however, leading to great uncertainty in how dissolved iron in subglacial runoff fits within the Southern Ocean iron budget. The measurements that have been made suggest a wide range of solute concentrations and oxidation states. For example, Lake Vostok is inferred to be low in solute concentration (Wadham et al., 2010) and primarily oxidized (McKay et al., 2003), as is Subglacial Lake Whillans (Michaud et al., 2017); conditions which do not favor high dissolved iron content. In contrast, subglacially derived water sampled at Blood Falls in Taylor Valley was reduced and highly concentrated in dissolved ions,

including iron (Mikucki et al., 2009; Lyons et al., 2019) and silica (Mikucki et al., 2004, 2015; Lyons et al., 2019). In these settings, small fluxes of groundwater discharge containing the concentration of solutes observed in Blood Falls, for example, could provide a significant pulse to coastal ecosystems (Mikucki et al., 2015). In the absence of an understanding of submarine groundwater discharge, the Southern Ocean budget of nutrients remains primarily unresolved. For example, current Southern Ocean Si budget calculations do not include the potential for subglacial discharge (Tréguer, 2014). The influx of this nutrient, like iron, could also be significant. The concentration of silica in Blood Falls was measured to be 484 μM Si; (Lyons et al., 2019), which is comparable to the concentration in the longest river in Antarctica, the Onyx River (Green et al., 2005).

Fast flowing ice, as found in Antarctic ice streams and outlet glaciers, is of particular interest to glaciologists, who, being interested in contribution of fast flow features to rapid sea level rise, preferentially drill and sample such dynamic ice sheet settings, e.g., Reference (Tulaczyk et al., 2014). Fast glacier flow, however, can generate high basal melt rates through shear heating (Joughin et al., 2002). Thus, our understanding of subglacial hydrology and aqueous geochemistry, when based mostly on borehole samples and observations, may be biased toward wetter, more dilute, and higher meltwater flux conditions. In this paper, we argue that high salinity SGD may originate from underneath glaciers and thawed permafrost zones along the coastal zone of Southern Victoria Land, Antarctica. Here, as in other parts of coastal Antarctica, the ice sheet margin is thin and more prone to experience little or no basal melting, or even

basal freezing (Pattyn, 2010). Basal freezing may concentrate soluble ions in the remaining waters ('cryoconcentration'), resulting in a subglacial hydrology that is starkly different than the 'classic' ice stream subglacial hydrology; here water generation and flux rates are small but solute concentrations are high. Slowly recharged hydrogeologic systems, such as would be expected in these coastal margins, would tend to have longer water residence times and, hence, may experience significant uptake of solutes due to extended water-rock interactions. This process, in addition to cryoconcentration, may be responsible for the high solute concentration observed in the brines in our study region (Mikucki et al., 2009; Lyons et al., 2019). We postulate here that hypersaline brines, detectable as subsurface electromagnetically conductive regions, flow to the ocean floor adjacent the McMurdo Dry Valleys (MDV) region of East Antarctica and deliver these acquired solutes. We estimate potential water and nutrient fluxes from these systems, particularly fluxes of iron and silica, to the coastal ecosystem.

SETTING AND METHODS

The MDV represent the largest ice-free region of Antarctica (Levy, 2013). The region contains several major, relatively ice-free valleys that open to the ocean (Figure 1). Despite perennial cold, hyper-arid conditions (Doran et al., 2002) liquid water exists at the surface in ice-covered lakes, seasonal streams and shallow groundwater systems (Levy et al., 2011). The largest valleys are former fjords that were inundated by the sea during the Neogene (Sugden et al., 1995). Much of the liquid in the MDV lake basins

exists as brine. There is also evidence of subsurface liquid. Blood Falls is a subglacial outflow of hypersaline brine at the terminus of Taylor Glacier in Taylor Valley (Keys, 1979). Multiple lines of evidence show this brine to be subglacially sourced (Mikucki et al., 2015; Foley et al., 2015). Geochemistry of brine collected at Blood Falls suggests cryoconentrated seawater with modification from rock-water interaction and evaporation (Keys, 1979; Lyons et al., 1999, 2019; Mikucki et al., 2009). The brine from Blood Falls also hosts a metabolically active (Mikucki et al., 2009) and diverse microbial community that is distinct from the surrounding glacier ice (Campen et al., 2019). Together with the extended rock-water interactions, the metabolic activity of microorganisms can facilitate mineral weathering in the subsurface, leading to high solute loads in some groundwaters. Blood Falls brine is hypersaline and rich in reduced iron (97% of iron species exist as Fe(II)) (Mikucki et al., 2009). Recent geophysical surveys have provided evidence that Blood Falls is the surface expression of a deeper, regional salty aquifer (Mikucki et al., 2015; Foley et al., 2015; Badgeley et al., 2017). Currently, Blood Falls is the only known surface discharge of Antarctic subglacial waters and therefore provides insight into the chemistry and biology of other potential subsurface brines observed in the MDV (Mikucki et al., 2015).

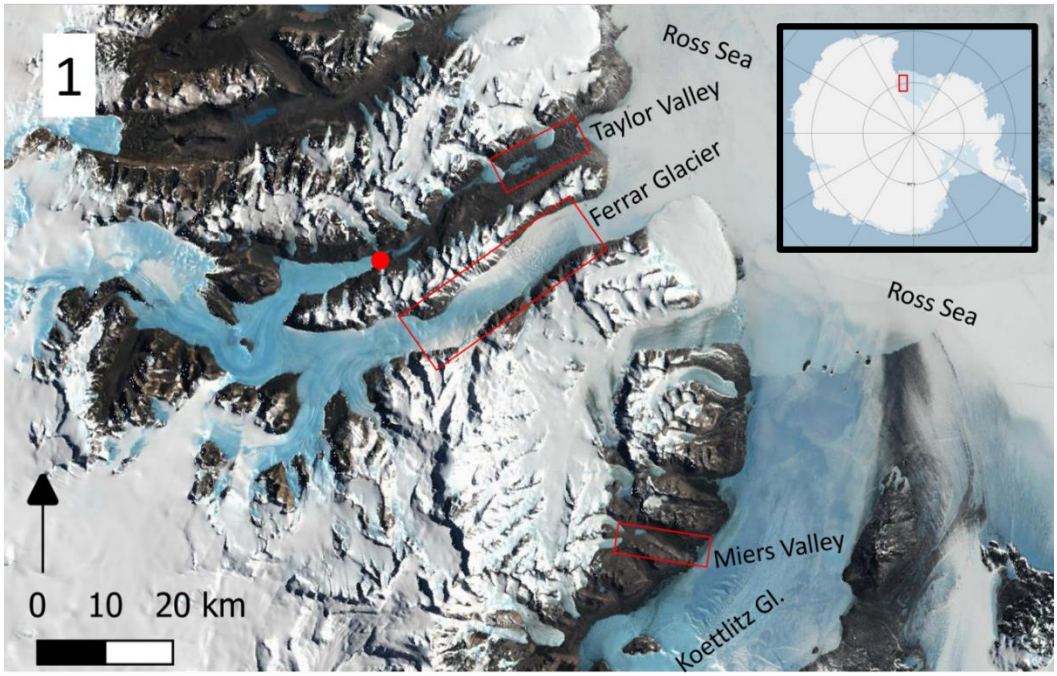

Figure 2.1. The McMurdo Dry Valleys Region Landsat Image of Antarctica (LIMA) high-resolution virtual mosaic (Bindschadler et al., 2008). The red dot denotes the location of Blood Falls at the terminus of Taylor Glacier. Inset shows the study region (red box) on a map of Antarctica.

An airborne electromagnetic (AEM) survey was flown in the MDV region in November 2018 using the SkyTEM312 system, as a follow up to a proof-of-concept 2011 AEM survey (Dugan et al., 2015; Mikucki et al., 2015; Foley et al., 2015). The SkyTEM312 system is an airborne transient-electromagnetic (TEM) sensor and consists of a rigid frame approximately 20 by 30 m in dimension on which the various system components are mounted. The entire system is suspended and flown beneath a helicopter allowing efficient data collection over extensive regions. It employs a dual moment transmitter with an area of 342 m^2. For the low-moment, the transmitter coil has 2 turns, a peak current of ~6 amps (A), and a repetition frequency of 210 hertz (Hz).

For the high-moment, the transmitter coil has 12 turns, a peak current of ~110 A, and a repetition frequency of 30 Hz. The use of a dual moment transmitter balances high-resolution in the shallow subsurface with large depth penetration (Sørensen and Auken, 2004), where the subsurface can be imaged to depths up to ~600–700 m in certain conditions, such as when a conductive aquifer underlies resistive materials like frozen ground or glaciers. The AEM system flown in 2018 has significant improvements over the 2011 system including larger transmit moments and a receiver with improved sensitivity. Together these advances translate to an improved depth penetration/resolution, as well as an aerodynamic frame capable of achieving greater flying speeds of ~80–110 km/h. The collected low and high-moment data presented here included time gates from 26 μs to 1.39 ms and 392 μs to 10.7 ms, respectively.

TEM measurement involves energizing a transmit loop (i.e., ramping a current up to a peak value) and then ramping down the current in the transmit loop as rapidly as possible. When ramping the current down, a time-varying magnetic field is produced in the subsurface which induces eddy currents that propagate downwards and outwards away from the sensor. These eddy currents in turn generate a secondary magnetic field. The time variation of the secondary magnetic field is measured using a receiver coil mounted on the frame flown beneath the helicopter. The decaying secondary magnetic field produces decaying voltage signals. Further details concerning the TEM method are in Chapter 6 of Kirsch.

The result of an AEM survey is a data volume consisting of suites of measured EM field decay curves collected along densely sampled profiles. The raw data are used to

constrain inverse models of subsurface electrical resistivity in the surveyed area. In this work, AEM data is inverted using a laterally constrained 30-layer inversion (Auken and Christiansen, 2004) implemented within the Aarhus Workbench software. Resistivities produced using a smooth inversion scheme are presented here. The resulting images of subsurface resistivity are presented as 2D depth slices, where the resistivity structure along a profile is visualized using a colormap (where the x- and y-axes represent distance along the profile and depth, respectively). In the presented profiles, the depth of investigation (DOI) is calculated using the approach outlined in (Christiansen and Auken, 2012). Data below the depth of investigation are displayed as semi-transparent, and the resistivity profiles beneath these depths are not interpreted because it is considered unreliable. Where the subsurface resistivity structure at any depth cannot produce a signal that exceeds the noise level of the instrument, the data are culled and no models are inverted. In these cases the subsurface can be considered to be very resistive down to the depth of investigation. In a high polar desert most near-surface materials (e.g., glacier ice, frozen ground) have very high electrical resistivity. Hence, the AEM system excels at detecting liquid water in this environment, particularly high-salinity, low resistivity liquid brines. In cold regions, where production of authigenic clays during chemical weathering of silicates is slow, electrical resistivity is largely a function of the presence or absence of liquid water, which carries electrolytic ions. In our study region, the majority of liquid water present exists as a cryoconcentrated brine either at the surface or at depth. The process of cryoconcentration transfers water molecules from liquid phase to solid phase, while

largely excluding dissolved ions from the newly formed ice crystals and concentrating them in the remaining liquid. Hence, cryoconcentration enhances the electrical contrast between solid and liquid phases of water. Cryoconcentrated brines, in turn, exist as a liquid at temperatures well below 0^{o}C and therefore can occur closer to the surface than would be possible for a freshwater groundwater system. In terms of electrical resistivity, subsurface brines correspond to low resistivity anomalies in the resistivity profiles. In contrast, subsurface regions containing no unfrozen water/brine, such as glaciers or permafrost, appear as areas of high resistivity.

An airborne electromagnetic platform is very well-suited to subsurface mapping in Antarctica. The surface is cold and arid, consequently a ground-based DC resistivity system would have difficulty achieving electrical contact with the surface. An inductive electromagnetic system (such as the SkyTEM312) does not require direct electrical contact with the ground. The absence of direct ground contact (both in terms of electrical contact and in respect to the fact that the system is suspended in air) is also valuable in protected areas where a ground-based survey risks disturbance of environmentally sensitive areas. An airborne platform also allows for rapid and dense data collection. An expansive AEM dataset, like the one collected by members of this team in November 2018, can provide insights into regional-scale hydrogeology of the MDV. To achieve similar coverage using ground-based methods would be infeasible given constraints on time, logistics, labor, safety considerations, and environmental accessibility.

Unlike a ground or sea-based DC survey, the AEM system cannot penetrate to great depths beneath seawater, as the highly-conductive medium strongly attenuates the signal as it propagates through the seawater. However, in Antarctica, the presence of sea ice limits the practicality of performing an off-shore DC survey. Another important distinction between DC and TEM surveys is that the greatest penetration occurs near the center of the profile for the DC survey, reducing to shallower depths near the edges of the profiles. In contrast, the TEM survey, even at a single site, can penetrate to depths up to 600–700 m depending on subsurface resistivity structure. As a result, AEM surveys can maintain large penetration depths all the way to the coastal margin. Note that the employed inversion of AEM data is based on 1D-physics for the forward model, which limits the ability to describe strongly 3D resistivity structures. One example of such a 3D-effect occurs at the coastal margins when the survey is flown perpendicularly to the coast. In locations where strong 3D-effects are identified during data processing stages, the data is culled and excluded from subsequent inversions (i.e., it does not influence the displayed profiles). Typically, this requires culling data roughly 150–250 m on either side of the coast.

RESULTS AND DISCUSSION

We collected approximately 3500 line kilometers of AEM data during 11 days of production. This survey spanned inland and coastal areas; one major focus was the connection between previously identified terrestrial brine aquifers and the ocean. We

identify three representative settings where subsurface brines are in contact with ocean water and may be exchanging through SGD:

(1) Lower Taylor Valley, where Lake Fryxell is connected to a deeper aquifer through a talik (unfrozen region) beneath the lake. This aquifer connects to the Ross Sea. This system is overlaid by permafrost between Lake Fryxell and the Ross Sea. (Figure 2A)

(2) Ferrar Glacier, where subglacial brines have an open connection directly into the Ross Sea. (Figure 2B)

(3) Miers Valley, where subpermafrost brines occur roughly at sea level but under a thin (and likely growing) layer of permafrost. (Figure 2C)

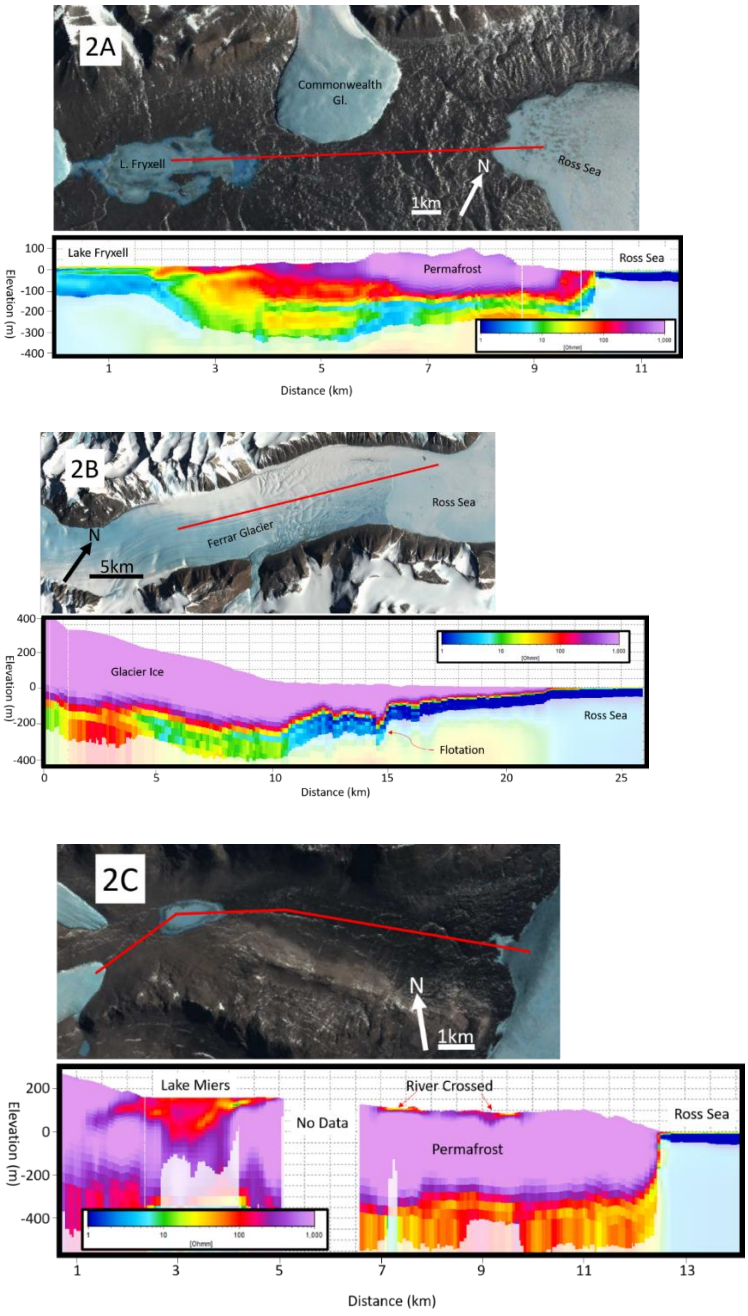

Figure 2.2. (**A**) AEM cross section of Lower Taylor Valley showing the connection between Lake Fryxell and the Ross Sea by a talik and conductive aquifer. Low resistivity regions are interpreted as liquid brines; (**B**) AEM cross section of Ferrar Glacier showing subglacial brine connecting to the Ross Sea; and (**C**) AEM cross section of Miers Valley. Brine can be detected underneath thick permafrost, and this brine appears to be in contact with the Ross Sea.

The extreme cold and aridity of Antarctica slow down hydrologic cycling of water and challenge our normal assumptions of the factors governing hydrogeologic processes. Here, most water exists as a slowly moving solid. Pattyn (Pattyn, 2010) estimated that the average basal melting rate beneath the Antarctic ice sheet is about 5–6 mm/year, which is an approximately two orders of magnitude less than average precipitation rates on other continents, of which only a portion may infiltrate to become groundwater. Because of this slow recharge rate, average residence times for groundwater in Antarctica can be expected to be a few orders of magnitude longer than on other continents, perhaps on the scale of millions of years in the slowest cycling portions (Mikucki et al., 2009). This, in addition to the cryoconcentration process discussed previously, would allow for extended water-rock interactions and acquisition of high solute concentration, which changes fundamental water properties. Indeed, in our study region, the groundwater must be saltier, colder and denser than seawater (McGinnis and Jensen, 1971; McGinnis et al., 1973, 1981, 1982); therefore the primary endogenic driver of SGD (buoyant instability) is shut off. Moreover, osmotic pressures are reversed from the conditions expected in a freshwater hydrogeologic system. Oceanic processes increasing efficacy of SGD in other settings are somewhat reduced because the near-perennial sea ice mutes wave pumping and wave set up. Tidal pumping remains a factor, but largely recirculates seawater (Prieto and Destouni, 2005).

While tidal pumping and wave processes can be enormous contributors to SGD flux exchange (Li et al., 1999), oceanic processes only recirculate and mix seawater with meteoric groundwater, mobilizing a modest amount of new solutes in every cycle. Subglacial water that is solute-rich (Skidmore et al., 2010), such as in the observed case for the source brine to Blood Falls (Lyons et al., 2019), has undergone prolonged concentration, rock-water interaction, and microbial modification which, as described above, has saturated the brine with ions including reduced iron (Mikucki et al., 2009) and silica (Lyons et al., 2019). Movement of this solute rich brine into proglacial systems can impact productivity and nutrient cycling by potentially providing limited nutrients such as silica and iron. Therefore, it is important to consider Darcian flow, which transports groundwater and its attendant solutes from areas of high hydropotential to low—typically toward the ocean. Darcian flow moves hypersaline brines from land to sea without recirculation of seawater, and therefore can deliver hyperconcentrated bioavailable nutrients like dissolved (reduced) iron from their long-term reservoir to the coastal zone. Darcian Flow is described by Darcy's Law:

$$Q = -K\,A\,\frac{dh}{dl} \tag{1}$$

where Q is the discharge (m^3/s), K is the hydraulic conductivity (m/s), A is the cross-sectional area across which discharge occurs (m^2), and dh/dl is the hydraulic head gradient (unitless, change in hydraulic head over distance, both in the units of length) (Freeze and Cherry, 1979).

Order of magnitude estimates of Darcian Flux can be derived for the settings observed in our study region (e.g., Figure 2A–C). Hydraulic conductivity can vary by many orders of magnitude and is particularly poorly constrained in this setting, rendering other uncertainties in gradient or area moot. Both the Ferrar Glacier and Taylor Valley represent former Miocene age fjords filled with marine diamictons and glacial drift (Sugden et al., 1995). We estimate the hydraulic conductivity using Hazen's Relationship (Hazen, 1892; Salarashayeri and Siosemarde, 2012):

$$K = C\,(D_{10})^2 \qquad (2)$$

where C is an empirical constant (typically ~1 to report K in cm/s), and D_{10} is the is the diameter of the finest 10% of grains (in mm). Using the grain size records of Dry Valley Drilling Project (DVDP) boreholes (Powell, 2013), we estimate that a representative hydraulic conductivity of the brine carrying sediments could be of order 10^{-8} m/s. This estimate is in line with tabulated ranges of hydraulic conductivity in glacial tills (Freeze and Cherry, 1979; Domenico and Schwartz, 1990), although it should be noted that conductivities can range over many orders of magnitude, and can be greatly enhanced by the presence of fractures. In a bulk flow setting, preferential flow through zones of higher conductivity may enhance the overall conductivity; similarly, clay or ice rich zone decrease conductivity. Drilling in the MDV has resulted in underpressurized and overpressurized wells, indicating heterogeneity in conductivities (McGinnis, 1979; Falconer et al., 2008). Without direct measurements beyond grain size and given the high sensitivity (power 2) to that grain size, we suggest that our estimate of hydraulic

conductivity at 10^{-8} m/s should be considered only accurate to within an order of magnitude (i.e., between 10^{-7} and 10^{-9} m/s).

Surface Slope Driven Darcian Flow

Most MDV aquifers are confined by permafrost over at least some of their area. An example of this is seen in Lower Taylor Valley from Lake Fryxell to the Ross Sea (Figure 2A), where a subsurface aquifer connects Lake Fryxell to the Ross Sea by a 20 m head drop (dh) over 6500 m (dl), or or a dh/dl of 0.003. Assuming the average density of the water column from Lake Fryxell surface to aquifer basement is more dense than sea water, the dh/dl will be a little greater than this. Based on the presence of the lowest resistivities, the aquifer has a saturated thickness of 50 m and is about 2000 m wide, resulting in a, conservatively estimated 100,000 m^2 cross sectional area (A). The estimated flux (Q) is therefore of the order of 100 m^3/year (between 10 and 1000 m^3/year when using the range for hydraulic conductivity estimated above).

Changes in lake level can significantly change the local hydraulic gradient. MDV lakes have fluctuated dramatically in the Quaternary (Hendy, 2004). The Fryxell basin, which is currently occupied by Lake Fryxell at close to sea level, may have been occupied by a proglacial freshwater lake (Lake Washburn) at the end of the Last Glacial Maximum that existed up to 78 masl (contained by a saddle after the Ross Ice Sheet retreated) (Hall et al., 2000; Hendy, 2004). This would have roughly quadrupled the hydraulic gradient toward the ocean (i.e., 380 m^3/year as our best estimate or 38–3800 m^3/year using the range of hydraulic conductivities). Conversely, a postulated late Holocene desiccation of Lake Fryxell (Lyons et al., 1998) could have dropped the

elevation of the lake below sea level, increased the salinity due to evapoconcentration, and completely reversed the gradient, driving groundwater flow inland and creating submarine groundwater recharge.

In a subglacial confined aquifer, such as under the Ferrar Glacier (Figure 2B) the horizontal head gradient, dh/dl, can be estimated as the drop in head over a distance. Without direct measurement, this is difficult to know with certainty, but an upper bound is to assume the glacier is at flotation and that the hydropotential of basal water is 90% of the ice thickness (Cuffey and Paterson, 2010). In the case of Ferrar Glacier, over the length scale over which brine is detectable, the data show a maximum drop of 300 m over 12,000 m, or 1 in 40. The saturated zone is about 4000 m wide and 50 m thick, or about 200,000 m^2 in cross sectional area. Due to the higher gradient in hydraulic head, a glacier like Ferrar could produce SGD of the order of 1500 m^3/year (or a range of 150–15,000 m^3/year). Ferrar Glacier is moderately steep and marine terminating, making it the most representative setting for East Antarctica coastal margins out of the three example settings chosen here from our study area.

Pressurized, confined aquifers can even be found in the absence of any visible slope. Overpressurized brines have been found by boreholes throughout the MDV region on land (McGinnis, 1979; Dugan et al., 2015) and underneath the McMurdo Sound (Falconer et al., 2008). Layers of frozen permafrost, as well as low permeability clay-rich layers, are capable of confining overpressurized aquifers and thus extending hydraulic head some distance from the up-gradient reservoir. This could allow transport of SGD farther out to sea with prolonged sediment-water interaction, allowing for the

delivery of reduced iron to greater distance offshore before it is oxidized by ocean water and becomes insoluble.

Volume Expansion Driven Darcian Flow Due to Permafrost Growth

In Miers Valley (Figure 2C), thick permafrost overlies brine in a small valley that opens to Koettlitz Glacier and the ocean. The surface slope is small, but the expansion of downward-freezing permafrost could be driving some groundwater flux to the ocean. A ~30 m higher sea level in the MDV region during the mid-Holocene could have exposed higher valley sediments to saltwater (Hall et al., 2004), which has since been freezing down at rates currently estimated to be mm per year (Osterkamp and Burn, 2003). The volume expansion of water upon freezing can pressurize groundwater and expel it toward the ocean without any gravity-driven head. Since volume expansion of water upon freezing is about 10%, freezing at rates of 1 mm/year should 'push' groundwater out at rates of ca. 0.1 mm/year. For a valley that is about 10 km long and 3 km wide, this would result in a groundwater outflow of the order of 3000 m^3/year. This process has the potential to link SGD output from ice-free regions of coastal Antarctica to climate changes, in that it would tend to occur transiently during periods of climate cooling and associated permafrost growth. Additionally, there is evidence that similar to Lake Fryxell basin, Miers Valley was occupied by a large paleolake at the end of the Last Glacial Maximum (Hendy, 2004). This would significantly alter the hydraulic gradient towards the ocean and the flux of SGD.

Darcian Flow as a Transmitter of Nutrients on a Continental Scale

Estimated fluxes of Darcian SGD are low in the MDV, due to low hydraulic conductivities, low driving gradients, and slow freezing. For example, the specific discharge of SGD at Ferrar Glacier is estimated to be about 1‰ of the ice discharge at the terminus. However, brines in the region are hyper-concentrated with ions (Mikucki et al., 2004, 2009; Lyons et al., 2019), allowing for relatively high solute transport nonetheless. In contrast to West Antarctica, interior East Antarctica is predicted to have overall lower basal melting and is largely surround by zones of net freezing near the coasts where the ice is thin but surface temperatures are cold (Pattyn, 2010). This 'confining ring' of cold-based ice sheet margin helps to cryoconcentrate groundwater before it reaches the coast (Figure 3). Thus, a low flux, high concentration groundwater scenario may be representative of much of coastal East Antarctica, and some parts of West Antarctica (e.g., Mary Byrd Land).

Recently, the first observationally constrained estimate of groundwater (as a combination of submarine and subglacial discharge) flux to the ocean from Antarctica was made in the West Antarctic Peninsula (Null et al., 2019); no estimates have been made in locations representative of other glacial and climatic regimes on the continent. Pattyn (Pattyn, 2010) modeled melting and freezing at the base of Antarctic Ice Sheet and estimated that 65 km^3/year of liquid water is produced at the ice base, equivalent to 5.3 mm/year melt continent-wide. In Antarctica, this basal melt is the equivalent to liquid precipitation on other, non-ice-covered continents. On average, groundwater recharge rates on other continents represent ca. 30% of total precipitation rates (Döll and Fiedler, 2007). In the absence of other constraints, we assume the same ratio and

obtain ca. 20 cubic kilometers per year as an approximate estimate of the overall Antarctic groundwater recharge rate. The remaining 45 cubic kilometers per year of meltwater is assumed to run off relatively rapidly through systems of subglacial streams and rivers (Priscu et al., 2008). Assuming no significant change in groundwater storage, this 20 km^3/year represents the approximate annual continent-wide groundwater discharge rate, too. The total volume of shallow, active groundwater in Antarctica is estimated to be of the order of 1 million km^3 (Priscu et al., 2008); which at a discharge rate of 20 km^3/year requires a residence time of approximately 50,000 year. The groundwaters detected in our study area are probably much older than 50,000 year, given the timescales required to achieve such high salinity through rock-water interaction and cryoconcentration. It has been hypothesized that they have remained subglacially isolated for a few million years (Mikucki et al., 2009). Using our prior estimates of subsurface brine volume in the Taylor Valley (ca. 0.3–0.6 km^3 assuming 20–40% of sediment porosity (Mikucki et al., 2015)), this kind of residence time would be compatible with SGD flux rates from this valley of ca. 100–200 m^3/year, which is reasonably close with our independently calculated modern Darcian flux of groundwater. Hence, we infer that the subsurface brines imaged by our AEM survey represent the fraction of Antarctic groundwater that overturns significantly more slowly than average and has residence time closer to millions of years rather than 50,000 years. Absent any constraints, we assume for illustration purposes that these old, concentrated, sluggish groundwaters represent 5% of the 20 km^3/year groundwater flux on the continent. This estimate is, of course, chosen partly of convenience to estimate

that 1 km^3/year of hypersaline groundwater flows to the ocean. It can serve as reference value for future researchers of this problem, who with further data may have reason to estimate saline groundwater flux as greater or less than (the order of) 1 km^3/year.

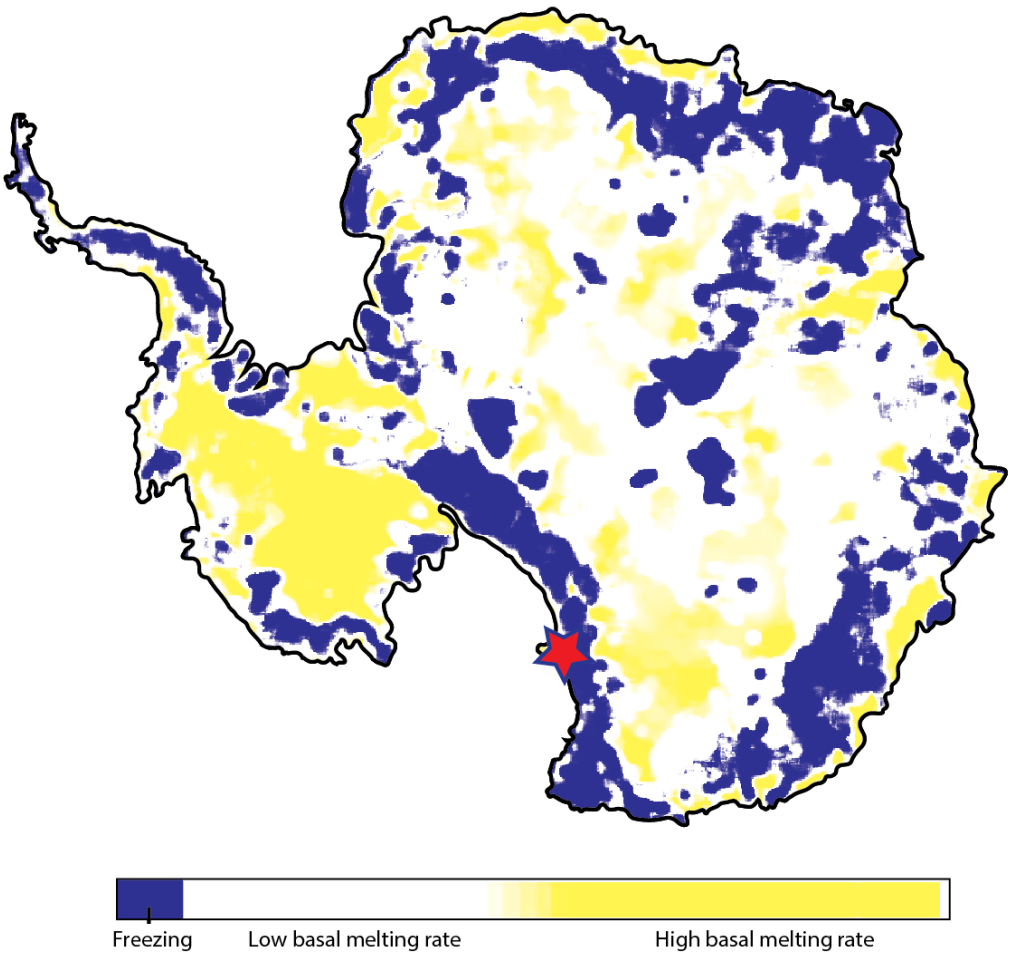

Figure 2.3. Basal melting conditions in Antarctica, adapted and simplified from Reference (Pattyn, 2010). Freezing conditions at the base are indicated by blue and high (above average) melting rates (<6 mm/year) are indicated by yellow. West Antarctica has relatively overall basal melt rates, while East Antarctica has lower melts rates. The margin of the East Antarctic ice sheet contains extensive zones of net freezing, and this 'confining ring' is proposed by us to be a zone of cryoconcentration near the coast. The red star marks the study area.

Past analyses of subglacial nutrient flux (Wadham et al., 2010, 2013) have focused on the relatively highly dynamic subglacial hydrologic system, in which basal meltwater fluxes are high at the interface of ice with underlying geology, but waters that have been sampled from such settings (Christner et al., 2014) are many orders of magnitude more dilute than the subsurface brines found in the MDV. Wadham and others (Wadham et al., 2013) suggested an upper bound on iron flux by taking high concentrations from Blood Falls brine (Mikucki et al., 2009) and applying them to the maximum Antarctic runoff suggested by Pattyn's (Pattyn, 2010) basal melt model. Instead, we propose that the conditions for high subglacial hydrologic flux are necessarily opposed to having a high concentration of dissolved ions, and that it is more reasonable to use our estimated slow (1 km^3/year) SGD fluxes with the high concentration brines. Wetter, higher flux systems will have shorter water-rock interactions and are reasonably expected to be more dilute.

We present estimates of flux of Fe and Si through such hyperconcentrated SGD in Table 1, which is modeled after Table 2 in Reference (Wadham et al., 2013). We introduce new, direct englacial samples of the Blood Falls source brine from (Lyons et al., 2019), which are believed by the authors to be more representative than the Blood Falls outflow measurements reported by (Mikucki et al., 2009) and used by Wadham and others (Wadham et al., 2013). For comparison, we include fluxes as calculated by the maximum basal melting scenario, although we feel this is unrealistic, as discussed above. Such a scenario was presented as an upper bound by Wadham and others (Wadham et al., 2013). We estimate that coastal East Antarctica may receive on the

order of 170 Gg/year (based on Blood Falls outflow concentrations) to 20 Gg/year (based on englacial brine concentrations) of soluble iron through submarine groundwater discharge, with higher confidence in the lower value determined from more accurate englacial sampling. Interestingly, these values are very similar to Wadham's intermediate and low flux estimates, respectively, which use similar high flux, but assumes a lower solute concentrations more representative of deep glacial groundwater (Wadham et al., 2013). Similarly, we estimate that Si flux is closer to Wadham and others' (Wadham et al., 2013) low flux estimate, for the same reasons. This hints at the reciprocity between concentration and flux of subglacial fluids. We propose that these two endmember hydrologic systems (high flux, low concentration; and low flux, high concentration) should be studied in the future with recognition of their distinct geochemical and hydrologic characteristics and origins.

Table 2.1. Estimated fluxes of Fe and Si through continent-wide SGD, after Table 2 from (Wadham et al., 2013). Sources: Reported concentrations and calculated values from fields marked (a) are from Reference (Wadham et al., 2013); concentrations from fields marked (b) are from Reference (Lyons et al., 2019) and the unmarked calculated values are scaled after Table 2 from Reference (Wadham et al., 2013). (Wadham et al., 2013) cites and slightly rounds its Fe concentrations from Reference (Mikucki et al., 2009) and its Si concentrations from References (Gosselin et al., 2001; Kim et al., 2002).

Ion	**Concentration (μM)**	**Flux of Ions (Gg/year)**	
		At 1 km^3/year SGD	**At 65 km^3/year SGD**
Fe(II) (Blood Falls outflow, filtered to remove insoluble particulates)[a]	3000	170	11,000[a]
Fe (total iron, direct englacial sample, unfiltered)[b]	476	30	1700
Fe(II) (direct englacial sample, filtered to remove insoluble particulates)[b]	351	20	1300
Si[a]	600	17	1100[a]
Si[b]	484	14	900

CONCLUSIONS

AEM resistivity can rapidly detect brines in the cryosphere if they are present within 100s of meters of the surface. The MDV provide a good test case because they contain very concentrated brine largely unshielded by thick ice, making it easy to image areas of potential SGD. Before AEM surveys, observations of liquid groundwater in the MDV were limited to point observations from the DVDP borehole data (Cartwright and Harris, 1981), sporadic sampling of Blood Falls outflow (Keys, 1979; Mikucki et al., 2009) or the near-surface expression of its subglacial reservoir (Lyons et al., 2019), and shallow groundwater flows in the form of water tracks (Levy et al., 2011). Using AEM, Mikucki and others (Mikucki et al., 2015) showed widespread liquid brine in the MDV, but the 2011 survey had sparse spatial coverage along the coast. The 2018 AEM survey fills in gaps that not only confirms groundwater connection between terrestrial groundwater reservoirs and the ocean, but also allows us to estimate potential SGD fluxes, which is critical for understanding nutrient fluxes to the ocean. We estimate that approximately 1 km^3/year (~2% of total continent-wide basal melt) of hypersaline groundwater exits Antarctica as SGD and is chemically similar to that detected in the MDV. We predict that this slow, salty flux carries approximately 20 Gg/year of Fe and 14 Gg/year of Si to the Southern Ocean through SGD, particularly in East Antarctica, where the MDV are examples of the widespread net freezing at the coastal margin. This subglacial setting stands in marked contrast to the dilute, high flux conditions expected in most of West Antarctica, but is has the potential to be similarly as significant for nutrient transport.

Chapter 3: Mapping Geothermal Heat Flux Using Permafrost Thickness Constrained by Airborne ElectroMagnetic Surveys on the Western Coast of Ross Island, Antarctica

ABSTRACT

Permafrost is ubiquitous at high latitudes, and its thickness is controlled by important local factors like geothermal flux, ground surface temperature, and thermal properties of the subsurface. We use airborne transient electromagnetic resistivity measurements to determine permafrost thickness on the coast of Ross Island, Antarctica, which contains the active volcano Mt Erebus. Here, resistivity data clearly distinguishes resistive permafrost from the electrically conductive fluid-saturated materials underlying it. For our study, we define permafrost as frozen material with a resistivity >100 Ω-m; more conductive material contains a significant fraction of water or (more likely) brine. We observe that permafrost is very thin near the coast and thickens within several hundred meters inland to reach depths that are typically within the range of 300-400 m. We attribute the sharp near-shore increase of permafrost thickness to lateral heat conduction from the relatively warm ocean, possibly combined with seawater infiltration into the near-shore permafrost. We validate this result with a two-dimensional heat flow model and conclude that away from the thermal influence of the ocean, the local geothermal gradient and heat flux are about 45 ±5 °C /km and 90 mW/m^2 ±13 mW/m^2, respectively. These values are in line with published estimates in

the vicinity of Mount Erebus and within the actively extending Terror Rift, but do not reflect a strong heat flow anomaly from volcanic activity of Mt Erebus. Measurements made previously in the McMurdo Dry Valleys, on the other side of McMurdo Sound, tend to be a few dozens of mW/m^2 lower, likely reflecting its different tectonic setting on the uplifted rift shoulder of Transantarctic Mountains. Our study demonstrates a new approach towards constraining geothermal flux in polar regions using AEM data that can be relatively efficiently collected on regional scales where ice coverage does not exceed the penetration limits of the AEM device, which for the device used is about 500m under the favorable conditions in the study area.

INTRODUCTION

Geothermal heat flux (GHF) is a key constraint on Earth's crustal and near-surface evolution and history (Davies and Davies, 2010). It plays a particularly significant role in high polar environments where it helps to control the thickness of permafrost, distribution of groundwater, and motion of glaciers and ice sheets (Lachenbruch et al., 1982; McKenzie and Voss, 2013; Fisher et al., 2015; Begeman et al., 2017). Geothermal energy resources in high polar environments may play an increasing role in meeting future human energy needs (Ragnarsson, 2003), including its increasing utilization in support of polar research facilities (e.g., Kyle, 1990), although significant barriers to practical implementation at high latitude remain.

Despite the scientific and practical importance of constraining GHF in polar regions, obtaining measurements and estimates of this quantity is challenging due to

the technical difficulty and logistical barriers associated with drilling through permafrost and glacier ice in remote polar environments (e.g., Melles et al., 2011; Tulaczyk et al., 2014). Furthermore, it is increasingly recognized that polar environments need to be protected because they may contain uniquely adapted organisms and habitats subject to limited human disturbance (e.g., Doran and Vincent, 2011). Such environmental protection measurements increase the difficulty of borehole drilling and temperature gradient measurements in sensitive polar regions (Tulaczyk et al., 2015).

Here we present a geophysical approach towards mapping geothermal heat flux in a high polar environment using an Airborne ElectroMagnetics (AEM) survey of permafrost thickness at the western flank of the Mount Erebus volcano, Antarctica (Figure 1). This survey, which covered about 20km^2, was part of a larger 2011 campaign in the McMurdo Dry Valleys region which collected time domain EM data over 300 km^2 in total. Time domain EM methods are ideal interrogating the first several hundred meters of the subsurface while being small and light enough for an airborne package. The first such survey to use them in Antarctica (2011) detected liquid brines beneath glaciers and permafrost (Mikucki et al., 2015; Foley et al., 2015) and various lakes (Mikucki et al., 2015; Dugan et al., 2015) in the Dry Valleys. A 2018 follow up survey using an improved system found evidence of sub-permafrost submarine groundwater discharge (Foley et al., 2019) across a similar area.

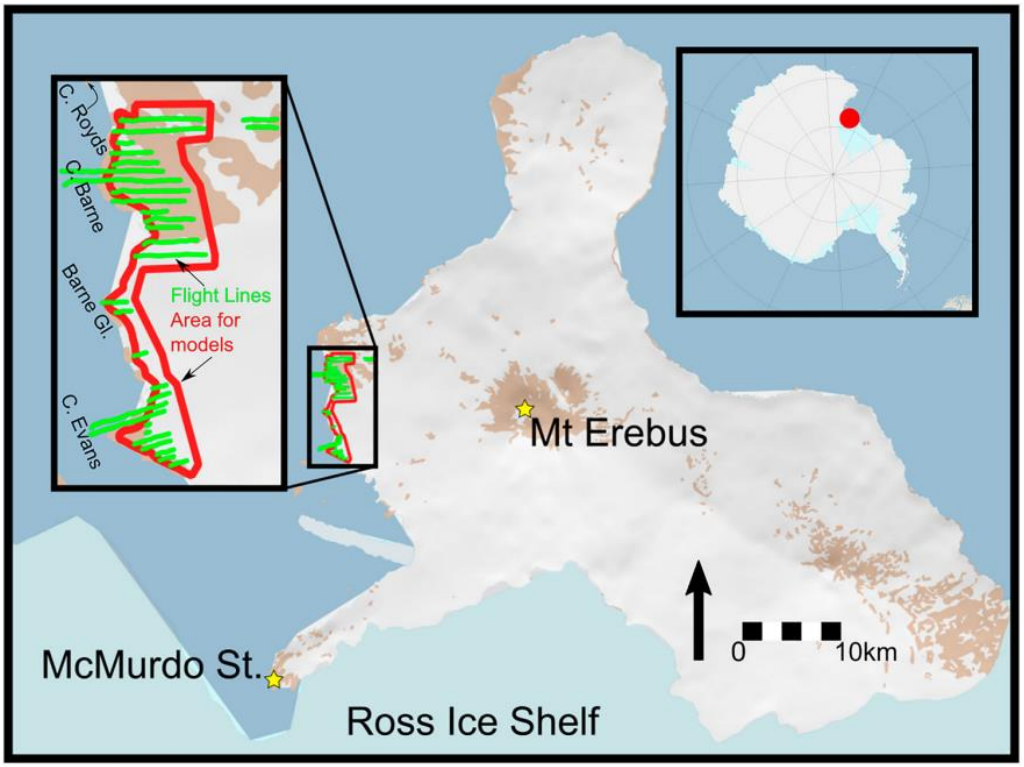

Figure. 3.1: Map of the field area. Ross Island is depicted in the main figure frame and the inset shows the location of survey flightlines in green. The northern flightlines cover the southern edge of Cape Royds & Cape Barne and the southern flightlines cover Cape Evans. In between, a few short lines cover the terminus of the Barne Glacier. The red outline marks the extent of data displayed in Figure 2. Measurements outside the red outline were either over water (limited DOI) or high residual, low signal measurements that were too far from the bulk of the data to use in our calculations.

Various other electrical techniques have been used in Antarctica across a variety of scales and regions. Direct current methods, which require physical and electrical contact with the surface, have been used to study the Antarctic ice sheets (e.g., Hochstein, 1967), ice shelves (e.g., Bentley, 1977) and on frozen ground in the Dry Valleys (McGinnis et al., 1973). Frequency domain methods, an electromagnetic technique closely related to time domain electromagnetics, have been used before in

Antarctica on both ground-based and airborne platforms, including to detect brine beneath permafrost (Ruotoistenmäki and Lehtimäki, 1997). Frequency domain EM is often used to measure Antarctic sea ice thickness (e.g., Worby *et al.*, 1999), including on helicopter borne packages (Rack et al., 2013). In the Arctic, helicopter borne systems are commonly used to measure sea ice with great accuracy (Pfaffling et al., 2007). Northern hemisphere permafrost is also measured with a variety of electromagnetic techniques (Hauck et al., 2001; Todd and Dallimore, 2002; Korhonen et al., 2009). Magnetotellurics, with their ability to image to great depth, have been used to investigate the magmatic system of Mt Erebus (Hill et al., 2017), the state of the bottom of the ice sheet through the lithosphere at the South Pole (Wannamaker et al., 2004) and the Transantarctic Mountains (Wannamaker et el., 2017).

This survey, a subset of the 2011 AEM campaign, covered the western coastal zone of Ross Island stretching from Cape Evans in the south to near (but not into) the edges of the Antarctic Specially Protected Areas ('ASPA') on Cape Royds in the North, and reached from a few hundred meters to a few kilometers inland. Permafrost is readily detectable in the AEM data because it represents a high-resistivity frozen layer underlain by a lower resistivity, fluid-saturated medium. For clarity, we use the term 'permafrost layer' to refer to the upper part of the subsurface in which solid ice exists in some or all interstitial space. By assuming that the permafrost is in steady-state and estimating its surface and bottom temperatures, we calculate the conductive temperature gradient through the permafrost layer and estimate GHF. Our GHF values fall around 100 mW m^{-2} which is close to the middle of the GHF range reported

previously for this region (Morin et al., 2010) and is consistent with our study area being on the flank of an active volcano (Parmelee et al., 2015) where surface volcanic rocks date to 70-90,000 years ago (Harpel et al., 2004).

METHODS

Airborne EM Resistivity

In late 2011 we measured subsurface electrical resistivity across the McMurdo Sound region (Mikucki et al., 2015) using a helicopter-borne time-domain electromagnetic (TEM) sensor, commercially known as SkyTEM (Sørensen and Auken, 2004). The SkyTEM system has a rigid frame approximately 20 m by 30 m in dimension on which a transmitter coil, TEM instrumentation, and receiver coil are mounted. The frame is suspended beneath a helicopter and measurements are conducted as the helicopter flies. The system used in this survey has a maximum transmitter moment of approximately 160,000 Am^2 and uses a dual moment transmitter that is capable of recording near-surface (10s of meters) resistivity with the low moment, and deep (100s of meters) resistivity with the high moment. Dual moment acquisition balances high-resolution in the near-surface with large penetration depths; low and high-moments in this case refer to signals collected following a current pulse of 9.5 A and 95 A, respectively. The TEM signal is produced by pulsing a current in the transmitter coil, which is shut off as rapidly as possible. During the current turn-off, a time-varying magnetic field is induced in the subsurface. This time-varying magnetic field generates eddy-currents in the subsurface, which in turn generate a

secondary time-varying magnetic field that can be detected inductively using a receiver coil mounted on the suspended frame. The amplitude and time-characteristics of the observed time-varying secondary field contain information about the electrical resistivity structure of the subsurface. Electrical properties of the Earth can be used to gain insight into subsurface geology; for example, permafrost regions have large resistivities while regions containing unfrozen brines have very low resistivities. Readers are directed to chapter 6 of Kirsch (2009) for a more comprehensive discussion of the TEM method. An alternative airborne EM method that has been previously employed at high-latitudes is frequency-domain electromagnetics (FEM) (Kovacs and Holladay, 1990; Multata et al., 1996; Haas et al., 2009; Ball et al., 2011; Minsley et al., 2012). TEM and FEM differ in data acquisition protocol, where FEM measurements continuously oscillate currents and measure signals while currents are still present in the transmitter coil. Both schemes are able to image the electrical properties of the subsurface. Relative performance of FEM and TEM systems is system dependent; however, the SkyTEM system employed in this work is able to provide both shallow and deep information and has in general much larger depth of investigation compared to the FEM system. FEM systems' penetration depths are limited by the lowest available frequency. Operation at low frequencies reduces signal to noise ratios and can increase instrumentation weight (Steuer et al., 2009). Further, at great depth, the secondary magnetic field can be a small fraction of the primary magnetic field. Because FEM systems transmit and receive simultaneously, distinguishing the two fields can be

difficult when the secondary field is weak; TEM systems sidestep this problem by measuring the secondary field when the primary field is off (zero) (Zhdanov, 2017).

TEM systems are particularly sensitive to conductive materials and can achieve maximum penetration (up to 400 - 600m in our survey) when conductive material is below resistive material. In this scenario, the deep conductive material generates a strong secondary magnetic field, and signal is not lost to attenuation within the resistive overburden. The collected TEM data were inverted using a spatially constrained inversion scheme (Auken and Christiansen, 2004; Viezzoli et al., 2008) in AarhusInv (Auken et al., 2014; Kirkegaard and Auken, 2015), which creates a quasi-3D resistivity model of the subsurface using a forward model that is based on 1D physics. Despite the 1D forward model, the spatially constrained inversion scheme imposes similarity amongst neighboring 1D models, allowing reproduction of 3D structures. In contrast to past results from the Dry Valleys that were collected using this SkyTEM system (Dugan et al., 2015; Mikucki et al., 2015; Foley et al., 2015), here we use a 'sharp' inversion, which prioritizes the production of models containing few layers of relatively homogenous intralayer properties (Vignoli et al., 2015). This results in sharp transitions between regions of contrasting resistivity, helping pinpoint horizons between neighboring layers. This inversion scheme is appropriate for the subsurface structure in our study region, which consists of high resistivity materials (glaciers, permafrost, sea ice) on top of conductive materials (saturated rock or sediments, saltwater lakes, seawater), where the strong geological stratification should coincide with similarly strong contrasts in electrical properties.

The presented inversion results are masked (i.e. not shown) beneath the depth of investigation (DOI) (Vest Christiansen and Auken, 2012). The DOI represents the depth to which the estimated resistivity profile has an appreciable impact on the data fit. Below the DOI, the estimated models cannot be discussed with great certainty as they are not well-constrained by the data. The DOI is reached within a few 10s of meters in seawater or highly conductive substrate but is 100s of meters deep when conductors lie beneath non-conductors, as in the case when permafrost or glaciers overlie saturated sediments. The reason for variable DOI is that the conductive seawater attenuates the TEM signal more rapidly (as a function of depth) than the non-conductive permafrost, thus allowing the system to image deeper when thick permafrost layers are present. More details on the system and processing for our Antarctic data are available in Foley et al (2015).

EM methods are useful in the cryosphere because changes in the phase of water (from liquid to solid) can correspond to orders of magnitude changes in electrical resistivity. TEM is well-suited to the targeted system in this work (permafrost overlying a conductive brine), in that the depth to the conductor can be well-constrained and the resistive overburden allows the system to penetrate deeper. Note that in regions of very thick permafrost or ice it can be difficult to generate a measurable signal, as the eddy currents produced in the resistive ice correspond to a very weak secondary field. As such, if the permafrost layer exceeds a certain thickness one can lose the ability to detect the presence of an underlying conductor. To enhance depth penetration in these

scenarios larger transmitter moments or lower internal noise receivers would be necessary.

Measuring Permafrost Thickness

Permafrost freezes from the top down which should be represented in EM-derived resistivities as a highly resistive (frozen) layer overlying a conductive (water saturated) layer. The measured bulk resistivity of this conductive layer depends on the resistivity of the fluid and the porosity of the material that contains the fluid. This can be estimated with an empirical relationship called Archie's Law:

$$\phi = \left(\frac{\rho_0}{\rho_b}\right)^{-1/m} \quad (1)$$

where ϕ is the porosity, ρ_0 is the bulk resistivity, ρ_b is the resistivity of the fluid and m is a 'formation factor' that represents the geometries of the pore network (Archie, 1950). Assuming that the fluids we measure have a resistivity similar to seawater, and assuming a moderate value for the formation factor, measured resistivities of 100 Ω-m and 10 Ω-m correspond to porosities of 6% and 19%, respectively. Despite the uncertainties in determining the porosity of a saturated sediment from resistivity alone, 100 Ω-m is a reasonable threshold to distinguish between permafrost and thawed material: it is too conductive to be permafrost or unweathered rock (Palacky, 1987), and has been shown to correspond to material transitions elsewhere in the region (Foley et al, 2015).

To estimate permafrost thickness, we determined the depth from the surface to the 100 Ω-m layer with the Aarhus Workbench software. Note that the depth to the permafrost/brine interface is well-resolved because of the strong resistivity contrast between these layers (and the thickness of the brine layer); significant changes to the estimated interface depth result in poorer data fits. We exclude any measurements acquired over the ocean, or, in limited cases, where the 100 Ω-m layer was not detected above the DOI.

Estimating Geothermal Flux

The simplest approach to estimating geothermal flux from permafrost thickness is to use (Osterkamp and Burn, 2003, based on their equation 1):

$$G \simeq K \frac{\Delta T}{Z} \qquad (2)$$

where: G is the geothermal heat flux in SI units (W/m^2), K is the thermal conductivity of permafrost (W/m/C), and ΔT is the temperature difference between the mean surface temperature and the freezing point at the bottom of the permafrost layer. Clearly, this simple equation is underlain by a number of assumptions. Firstly, this is a steady-state solution to a one-dimensional heat diffusion equation which implies that all of the quantities involved have not varied significantly over the period of time required to reach the steady state. A rough estimate of this equilibration time scale can be obtained by calculating the e-folding timescale, τ, for a one-dimensional heat diffusion problem for a layer of thickness Z:

$$\tau = \frac{Z^2}{D} \quad (3)$$

where D is the thermal diffusivity of the permafrost layer. In the absence of published values for thermal properties of phonolite, the primary rock in the study area, we use the diffusivity of 25.2 m^2/yr (8×10^{-7} m^2/s) for pure basalt (Hartlieb et al., 2015), the mineralogy of which has similar thermal properties (Horai and Simmons, 1969). We expect some interstitial ice in the permafrost layer; ice has a higher thermal diffusivity which would result in a shorter, hence less conservative, diffusive timescale. With the diffusivity of pure basalts, equation (3) yields an e-folding timescale of ~3,500 to ~6,500 years for Z of 300 to 400 m, as observed by us away from the coast (Figure 2). This period falls within the mid-to-late Holocene climate period during which long-term regional climate has been relatively stable, with a slight cooling of up to a few degrees towards the present time (Cunningham et al., 1999; Baggenstos et al., 2018). Hence, below we will assume that the permafrost thickness determined is in a steady state.

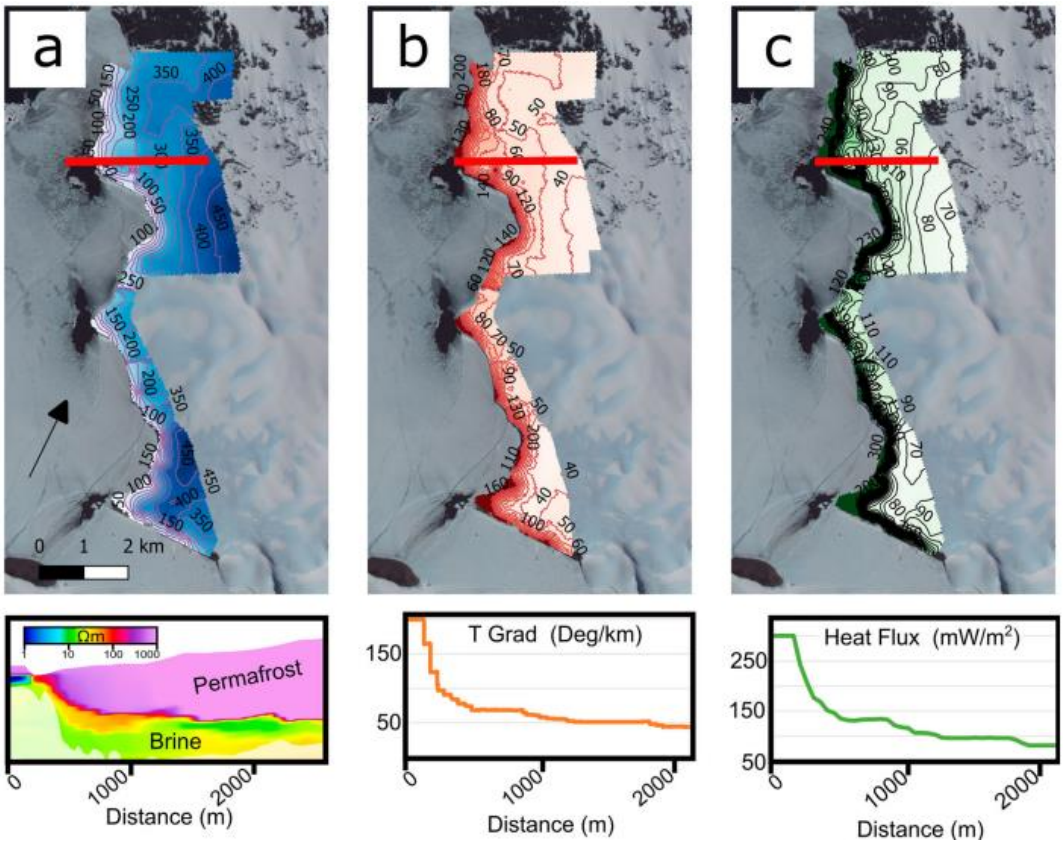

Figure 3.2. Results and calculations derived from EM measurements. In each, a cross section is shown along the same red line marked on the map. (a) Permafrost thickness, as calculated by depth from the surface to the 100 Ω-m layer. Contours are in 50m increments. Permafrost is very thin near the coast and increases in thickness more gradually inland. The cross section shows a profile through the resistivity data that were used to calculate permafrost thickness. The resistivity results are faded below the DOI. (b) The vertical temperature gradient from the bottom of the permafrost to the top. Contours are in 10 °C/km increments. Values are capped at 200 °C/km (near the ocean, where the permafrost is thin). (c) Vertical heat flux (mW/m^2) through the permafrost. Contours are in 10 mW/m^2 increments. Capped at 300 mW/m^2 near the coast where permafrost is thin.

In the absence of surface temperature measurements from our study area, we use the standard (2 m above ground) mean annual temperature of -20°C from this region (Monaghan et al., 2005; Doran et al., 2002) plus an offset of +2°C to account for ground temperatures being a few degrees warmer in high polar regions than the

corresponding mean annual temperature (e.g., Brown, 1966). This is consistent with surface temperatures projected from Dry Valleys Drilling Project (DVDP) borehole #3 on nearby Hut Point Peninsula (Decker and Bucher, 1982), a variety of temperature proxies from the McMurdo Sound Regions (Nichols and Ball, 1964) and observed mean annual air temperatures at McMurdo Station and Scott Base. For the temperature at the base of the permafrost we use the freezing point of seawater of ca. -1.9°C. We choose the freezing point of seawater rather than that of freshwater because we commonly observe very low electrical resistivities beneath the permafrost layer, e.g., ~10 Ω-m. Such bulk resistivity is difficult to obtain for freshwater saturated mafic rock, given that ~10 Ω-m is by itself a reasonable resistivity for groundwater. Using Archie's law (equation 1), this would imply that the material underneath the observed permafrost layer consists of unreasonably high fraction of groundwater. However, seawater has resistivity of 0.36 Ω-m and would yield bulk resistivity of saturated rock at sensible porosities of ca. 11-27% (Foley et al., 2015). The fact that our study area is in a coastal setting yields additional support to our assumption of seawater as the interstitial fluid beneath permafrost. With the mean annual surface temperature of -18°C and basal temperature of ca. -2°C, the temperature jump across the permafrost layer, ΔT, is ca. 16°C. This, together with permafrost thickness derived from our resistivity data allows us to calculate the geothermal gradient, which is then multiplied by thermal conductivity to obtain GHF. At low porosities thermal conductivity of basalts is slightly below 2 W/m/C while the thermal conductivity of ice itself is slightly higher than that (Horai, 1991). Here we use 2 W/m/C in our calculations of GHF, which is nearly the

same as the thermal conductivity observed at the middle of DVDP borehole #3 at Hut Point Peninsula (Decker and Bucher, 1982), which has a similar geology to our study area.

The greatest limitation of the one-dimensional heat flow model (equation 2) is that it cannot account for the lateral heat flow from the ocean towards land (Risk and Hochstein, 1974). We use a two-dimensional finite difference heat conduction model to account for the impact of steady-state horizontal heat transfer from the seafloor towards land. The bespoke MATLAB code solves the standard two-dimensional heat diffusion equation (Recktenwald, 2004):

$$\frac{\partial T}{\partial t} = D\left(\frac{\partial^2 T}{\partial x^2} + \frac{\partial^2 T}{\partial z^2}\right) \quad (4)$$

where t is time and x, z are the two spatial coordinates and D has been assumed to be uniform throughout the subsurface domain. The seafloor is prescribed seawater temperature of -2°C while land surface temperatures are assigned using sea-level temperature of -18°C and a regional lapse rate of 0.0098 °C/m from Doran et al. (2002). The lower boundary condition is constant heat flux, equal to the prescribed geothermal flux, which is assumed to be constant across the lower boundary of the model domain. Both lateral boundaries are set to have zero horizontal heat flow. Initial conditions are given by temperatures following a linear vertical temperature gradient, equal to the assumed geothermal gradient, from the bottom of the domain to the land surface or seafloor.

The numerical solver uses the explicit forward time, centered space technique (Recktenwald, 2004). The code was verified by solving numerically a Dirichlet two-dimensional problem on a rectangle and then comparing the model output to an analytical harmonic solution. Although the code solves a transient partial differential equation (4) given above, we use it to approximate a steady-state solution by running it for long enough so that no element within the numerical domain changes its temperature by more than 10^{-6} °C per year. This typically happens after more than 20,000 model years of holding all boundary conditions constant.

RESULTS AND DISCUSSION

Analytical Results of Permafrost Thickness and Heat Flux

Using the 100 Ω-m layer as an indicator of unfrozen ground, we found the thickness of permafrost (or glacier ice, at Barne Glacier) across ~20 km^2 of the coastal western flank of Mt Erebus (Figure 2a). Permafrost is very thin at or near the coast and increases in thickness rapidly over the first ~500 m distance from the coast. Permafrost must necessarily be thin at the coast because the ocean is steady at about -1.9 °C, whereas mean annual air temperature at sea level is about -18 °C (Doran et al, 2002; Monaghan et al, 2004). This results in very high horizontal heat flow from the ocean to nearby land (including permafrost and glaciers).

The thin coastal permafrost is reflected in our derived analytical models. Given the low resistivity, we assume the base of the permafrost is at -1.9 °C (the freezing

point of seawater) and the mean annual air temperature is -18 °C at sea level, with an environmental lapse rate of -6.5°C/km (Wallace and Hobbs, 2006). With these and the permafrost thickness, we calculate a vertical temperature gradient from bottom to top of the permafrost (Figure 2b). The temperature gradient is high near the coast due to the ocean's influence, but quickly settles to ~45 °C/km inland. To estimate the uncertainty on this geothermal gradient, we use the square-root-of-the-sum-of-squares assuming ~10% standard deviation on ΔT (ca. ±1.6 °C) and 5% standard deviation on Z (ca. ±20m for a 400m-thick layer). This estimate yields one standard deviation of 11%, which for the geothermal gradient of ~45 °C/km is ±5 °C/km.

We estimate vertical heat flux (Figure 2c) by assuming a thermal conductivity for basaltic material with ice filling its pores of 2.0 W/m C (based on Horai, 1991). The vertical heat flux is very high (>300 mW/m^2) near the coast, but settles to ~90 mW/m^2 inland, which is slightly high for the global average but reasonable for the region, which has high geothermal flux (Decker and Bucher, 1982), especially given the site's location on the flank of Mt Erebus, an active volcano, and in an area of regional extension. We add an estimated uncertainty in thermal conductivity of basaltic material of 10% (i.e., one standard deviation of ±2 mW/m^2) to the uncertainty in geothermal gradient calculated above to arrive at one standard deviation for GHF of 15%, i.e., about ±13 mW/m^2 for ~90 mW/m^2.

Past measurements of temperature gradient and heat flux from boreholes on Ross Island have noted the importance of heat flow from the ocean (Risk and

Hochstein, 1974). Even accounting for the ocean's influence, heat flow is variable in this region. Risk and Hochstein (1974) measured fluxes of 164 $mW/m^2 \pm 60$ mW/m^2 at Arrival Heights on Hut Point Peninsula (near McMurdo Station, see Fig. 1), which they attributed to recent volcanic activity on the peninsula. Our data come from an old part of the volcano with a complicated history of subsequent eruptive and intrusive events (Esser et al, 2004). Because our technique does not directly measure heat flux, but rather derives it from its effect on permafrost thickness, it may integrate heat sourced from older and more recent volcanic events, and thus be less biased by recent events, than a single borehole measurement could be.

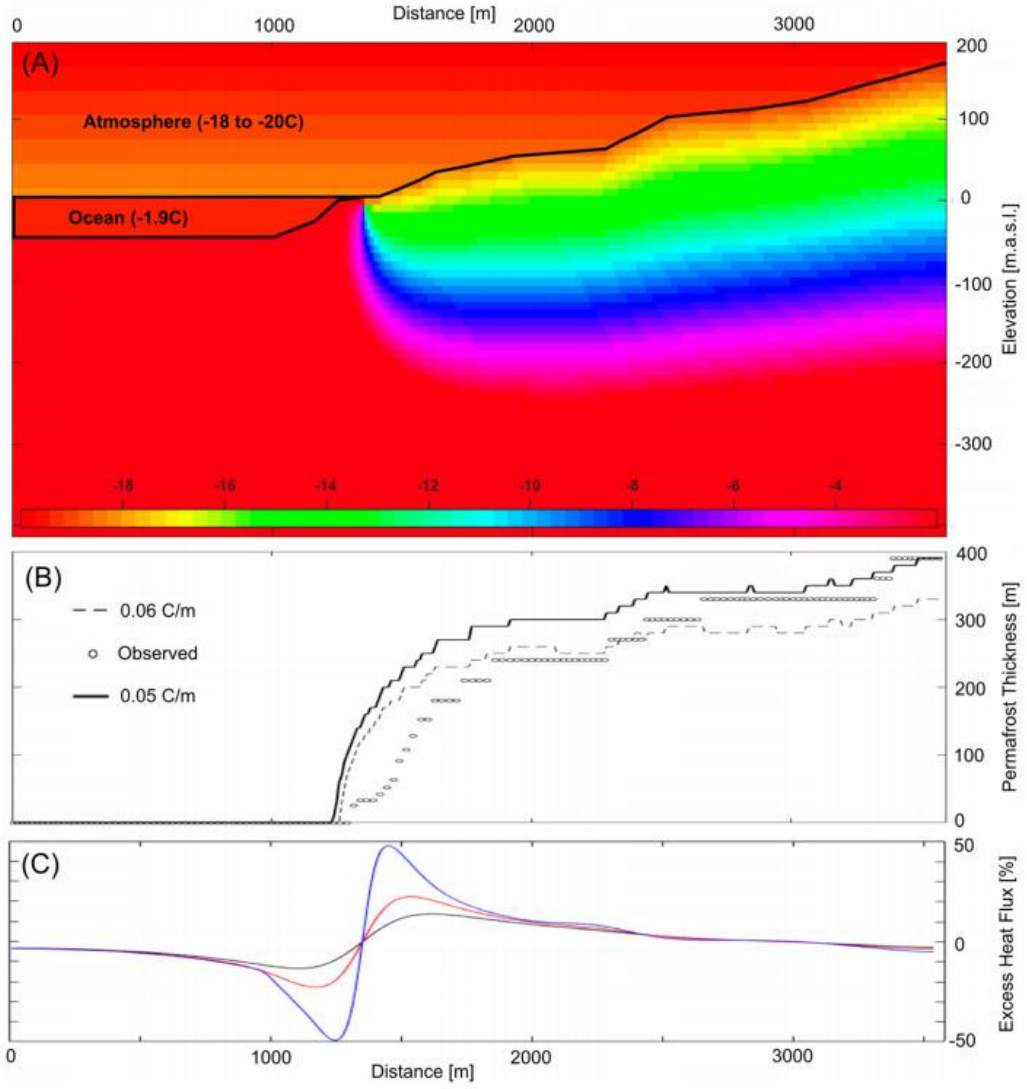

Figure 3.3. Temperature field from a two-dimensional heat flow model (a). The scale is chosen to show only the temperature range within the permafrost layer. Surface topography and the position of the coastline are taken from the same profile line shown above in Figure 2. This example is for assumed geothermal gradient of 60 °C/km. In panel (b) we show a comparison between the permafrost thickness distribution based on resistivity data (circles) and simulated permafrost thickness for two different values of geothermal gradient: 60 °C/km in dashed line and 50 °C/km in solid line. The lowermost pane (c) illustrates the high magnitude of excess vertical heat flux near the coastline. The excess vertical heat flux (in %) is calculated by subtracting the prescribed geothermal heat flux from the total vertical heat flow and then dividing the difference by the prescribed geothermal heat flux. The blue line shows the distribution

at 100m below sea level, the red line at 200m below sea level and the black line at 300m below sea level.

Our two-dimensional numerical heat flow model includes the effect of lateral heat transfer from the ocean on subsurface temperature distribution and calculated permafrost thickness (Figure 3a). Comparison of the permafrost thickness distribution derived from resistivity observations with the permafrost thickness predicted by the model shows, however, a significant mismatch (Figure 3b). The model predicts that the excess vertical heat flux caused by the heat exchange between land and the ocean should decay relatively rapidly inland, within a distance equal to about one to two permafrost thicknesses (Figure 3c). Beyond this distance the impact of conductive heat transfer between the land and ocean domains should be quite small. In our model, this leads to a very rapid rise of the permafrost thickness near the coastline so that the simulated permafrost thickness reaches half of its 'inland' value within just a few hundred meters from the coast. In contrast, the permafrost thickness based on the 100 Ω-m resistivity threshold rises only slowly over the first several hundred meters and then more rapidly further from the coast. We concur with the suggestion of Risk and Hochstein (1974) that near-shore permafrost on Ross Island, and perhaps in general, may be subject to seawater intrusion. As seawater intrudes into colder permafrost it may become cryoconcentrated into hypersaline brine, leading to development of a 'slushy' permafrost zone whose bulk resistivity drops below the 100 Ω-m threshold used here to define frozen ground.

CONCLUSIONS

While direct measurements of such fundamental geologic and geophysical properties like geothermal heat flux, groundwater salinity, and permafrost are desirable, practical or environmental considerations often render them unattainable in many polar locations. In a span of one day we collected EM resistivity data that allowed us to infer some of these properties and achieve results consistent with past measurements within the region. We estimate that the permafrost layer (here defined as near-surface material with bulk resistivity >100 Ω-m) is 300-400m thick in the region, except in the near-shore environment where it rapidly decays to nil at the coastline. This decay is partly due to lateral conductive heat flux from the warm ocean to the cold adjacent land. We also speculate that intrusion of seawater into coastal permafrost further impacts the properties of the nearshore permafrost, likely making it <100 Ω-m in resistivity. Our resistivity data do not suggest any positive evidence for local hydrothermal circulation (e.g., localized thinning of the permafrost layer) and do not necessitate invoking geologic control on subsurface resistivity distribution on the flank of this active volcano. Based on relatively low resistivities of the sub-permafrost material, we speculate that basaltic rocks are saturated by seawater in this coastal zone. The estimated geothermal gradient away from the coast is about 45 °C/km ±5 °C/km and geothermal flux ca. 90 mW/m^2 ±13 mW/m^2. These values are close to the middle of the range for other measurements of geothermal gradient and geothermal flux in this region (e.g., Morin et al., 2010).

REFERENCES

Archie, G. E. 1950. Introduction to petrophysics of reservoir rocks. AAPG Bulletin 34, 943–961.

Archie, G., 1950, Introduction to petrophysics of reservoir rocks, Am. Assoc. Pet. Geol. Bull., 34(5), 943–961.

Arcone, S.A., 2002, Stratigraphic profiling with ground-penetrating radar in permafrost: A review of possible analogs for Mars: Journal of Geophysical Research, 107, no. E11, 1–14.

Arcone, S.A., A.J. Delaney, M.E. Prentice, 2000, Stratigraphic profiling in the Antarctic Dry Valleys: 8th International Conference on Ground Penetrating Radar, Proc. SPIE 4084, 772–777.

Arcone, S.A., and K. Kreutz, 2009, GPR reflection profiles of Clark and Commonwealth Glaciers, Dry Valleys, Antarctica: Annals of Glaciology, 50, no. 9, 121–129.

Auken, E., A.V. Christiansen , C. Kirkegaard, G. Fiandaca, C. Schamper, A. Behroozmand, A. Binley, E. Nielsen, F. Effersø, N.B. Christensen, K.I. Sørensen, N. Foged, and G. Vignoli, 2014, An overview of a highly versatile forward and stable inverse algorithm for airborne, ground-based and borehole electromagnetic and electric data: Exploration Geophysics, doi:10.1071/EG13097.

Auken, E., A.V. Christiansen, 2004, Layered and laterally constrained 2D inversion of resistivity data: Geophysics, 46, no. 3, 752-761.

Auken, E., A.V. Christiansen, C. Kirkegaard, G. Fiandaca, C. Schamper, A.A. Behroozmand, A. Binley, et al. 2015. An overview of a highly versatile forward and stable inverse algorithm for airborne, ground-based and borehole electromagnetic and electric data. Exploration Geophysics 46, no. 3: 223–35. https://doi.org/10.1071/EG13097.

Auken, E., A.V. Christiansen, J.H. Westergaard, C. Kirkegaard , N. Foged, and A. Viezzoli, 2009, An integrated processing scheme for high-resolution airborne electromagnetic surveys, the SkyTEM system: Exploration Geophysics, 40, no. 2, 184-192.

Badgeley, J.A.; Pettit, E.C.; Carr, C.G.; Tulaczyk, S.; Mikucki, J.A.; Lyons, W.B. An

englacial hydrologic system of brine within a cold glacier: Blood Falls, McMurdo Dry Valleys, Antarctica. J. Glaciol. 2017, 63, 387–400.

Baggenstos, D., J.P. Severinghaus, R. Mulvaney, J.R. McConnell, M. Sigl, O. Maselli, J.R. Petit, B. Grente, and E.J. Steig. 2018. A horizontal ice core from Taylor glacier, its implications for Antarctic climate history, and an improved Taylor Dome ice core time scale. Paleoceanography and Paleoclimatology 33: 778–94.

Ball, L.B., B.D. Smith, B.J. Minsley, J.D. Abraham, C.I. Voss, M. Deszcz-Pan, and J.C. Cannia. 2011. Airborne electromagnetic and magnetic survey data of the Yukon Flats and Ft. Wainwright areas, central Alaska, June 2010, U.S. Geol. Surv. Open File Rep., 2011–1304, 28 pp.

Begeman, C.B., S.M. Tulaczyk, and A.T. Fisher. 2017. Spatially variable geothermal heat flux in West Antarctica: Evidence and implications. Geophysical Research Letters 44, no. 19: 9823–32.

Bentley, C. R. 1977. Electrical Resistivity Measurements On The Ross Ice Shelf. Journal of Glaciology 18, 15–35.

Berthling, I., B. Etzelmüller B., K. Isaksen, and J.L. Sollid, 2000, Rock glaciers on Prins Karls Forland. II: GPR soundings and the development of internal structures, Permafrost and periglacial processes, 11, no. 4, 357-369.

Bindschadler, R.; Vornberger, P.; Fleming, A.; Fox, A.; Mullins, J.; Binnie, D.; Paulsen, S.J.; Granneman, B.; Gorodetzky, D. The Landsat Image Mosaic of Antarctica. Remote Sens. Environ. 2008, 112, 4214–4226.

Bristow, C.S., P.C. Augustinus, I.C. Wallis, H.M. Jol, and E.J. Rhodes, 2010, Investigation of the age and migration of reversing dunes in Antarctica using GPR and OSL, with implications for GPR on Mars: Earth and Planetary Science Letters, 289, no. 1-2, 30–42.

Brown, R.J.E. 1966. Relation between mean annual air and ground temperatures in the permafrost region of Canada. In Proceedings of the permafrost international conference: Proceedings, NAS-NRC Publication No. 1287, 241–6.

Burnett, W.C.; Bokuniewicz, H.; Huettel, M.; Moore, W.S.; Taniguchi, M. Groundwater and Pore Water Inputs to the Coastal Zone. Biogeochemistry 2003, 66, 3–33.

Campen, R.; Kowalski, J.; Lyons, W.B.; Tulaczyk, S.; Dachwald, B.; Pettit, E.; Welch, K.A.; Mikucki, J.A. Microbial diversity of an Antarctic subglacial community and high-resolution replicate sampling inform hydrological connectivity in a polar

desert. Environ. Microbiol. 2019, doi:10.1111/1462-2920.14607.

Cartwright, K., and H. Harris, 1981, Hydrogeology of the Dry Valley Region: Dry Valley Drilling Project (ed L. D. Mcginnis): American Geophysical Union, Washington, D. C.

Cartwright, K.; Harris, H. Hydrogeology of the Dry Valley Region, Antarctica. Antarct. Res. Ser. 1981, 33, doi:10.1029/AR033p0193.

Christiansen, A.V., and E. Auken. 2012. A global measure for depth of investigation. Geophysics 77, no. 4: WB171–7. https://doi.org/10.1190/geo2011-0393.1.

Christiansen, A.V., E. Auken, and A. Viezzoli, 2011, Quantification of modeling errors in airborne TEM caused by inaccurate system description: Geophysics, 76, no. 1, F43–F52.

Christiansen, A.V., E. Auken, and K.I. Sørensen, 2006, The transient electromagnetic method: Groundwater geophysics: a tool for hydrogeology: Kirsch R. (ed.), Springer, Berlin.

Christner, Brent C., et al. "A microbial ecosystem beneath the West Antarctic ice sheet." Nature 512.7514 (2014): 310-313.

Creyts, T.T., and C.G. Schoof, 2009, Drainage through subglacial water sheets: Journal of Geophysical Research, 114, no. F4, F04008.

Cuffey, K.M.; Paterson, W.S.B. The Physics of Glaciers; Academic Press: New York, NY, USA, 2010; ISBN 008091912X.

Cunningham, W.L., A. Leventer, J.T. Andrews, A.E. Jennings, and K.J. Licht. 1999. Late Pleistocene-Holocene marine conditions in the Ross Sea, Antarctica: evidence from the diatom record. The Holocene 9, no. 2: 129–39.

Davies, J.H., and D.R. Davies. 2010. Earth's surface heat flux. Solid Earth 1, no. 1: 5–24.

De Baar, H.J.W.; Buma, A.G.J.; Nolting, R.F.; Cadée, G.C.; Jacques, G.; Tréguer, P.J. On iron limitation of the Southern Ocean: experimental observations in the Weddell and Scotia Seas. Mar. Ecol. Prog. Ser. 1990, 65, 105–122.

Decker, E. R., and G. J. Bucher, 1982, Geothermal studies in the Ross Island-Dry Valley region, p. 887–894. In C. Craddock [ed.], Antarctic Geoscience. The University of Wisconsin Press.

Decker, E.R., and G. Bucher, 1977, Geothermal studies in Antarctica: Antarctic

Journal of the United States, 12, no. 4, 102-104.

DeFoor, W.; Person, M.; Larsen, H.C.; Lizarralde, D.; Cohen, D.; Dugan, B. Ice sheet-derived submarine groundwater discharge on Greenland's continental shelf. Water Resour. Res. 2011, 47, doi:10.1029/2011WR010536.

Degenhardt, J.J., and J.R. Giardino, 2003, Subsurface investigation of a rock glacier using ground-penetrating radar: Implications for locating stored water on Mars, Journal of Geophysical Research: Planets, 108, no. E4, 8036.

Dickson, J.L., J.W. Head, J.S. Levy, and D.R. Marchant, 2013, Don Juan Pond, Antarctica: Near-surface CaCl(2)-brine feeding Earth's most saline lake and implications for Mars.: Scientific reports, 3, 1166.

Döll, P.; Fiedler, K. Global-scale modeling of groundwater recharge. Hydrol. Earth Syst. Sci. 2008, 12, 863–885.

Domenico, P.A.; Schwartz, F.W. Physical and Chemical Hydrogeology; John Wiley and Sons: New York, NY, USA, 1990.

Doran, P.T., and W.F. Vincent. 2011. Environmental protection and stewardship of subglacial aquatic environments. In Antarctic subglacial aquatic environments, Vol. 192, 149–57. Washington, DC: American Geophysical Union.

Doran, P.T., C.P. McKay, G.D. Clow, G.L. Dana, A.G. Fountain, T. Nylen, and W.B. Lyons, 2002, Valley floor climate observations from the McMurdo dry valleys, Antarctica, 1986–2000: Journal of Geophysical Research, 107, no. D24, 4772.

Doran, P.T.; McKay, C.P.; Clow, G.D.; Dana, G.L.; Fountain, A.G.; Nylen, T.; Lyons, W.B. Valley floor climate observations from the McMurdo dry valleys, Antarctica, 1986-2000. J. Geophys. Res. Atmos. 2002, 107, doi:10.1029/2001JD002045.

Dugan, H. A., Doran, P.T., Wagner, B., Kenig, F., Fritsen, C.H., Arcone, S. A., Kuhn, E., Ostrom, N.E., Warnock, J.P., and Murray, A. E., 2015b, Stratigraphy of Lake Vida, Antarctica: hydrologic implications of 27 m of ice: The Cryosphere, v. 9, p. 439–450, doi: 10.5194/tc-9-439-2015.

Dugan, H.A., Doran, P.T., Tulaczyk, S., Mikucki, J.A., Arcone, S.A., Auken, E., Schamper, C., and Virginia, R.A., 2015a, Subsurface imaging reveals a confined aquifer beneath an ice-sealed Antarctic lake: Geophysical Research Letters, v. 42, p. 2014GL062431, doi: 10.1002/2014GL062431.

Engel, Z., D. Nývlt, and K. Láska, 2012, Ice thickness, areal and volumetric changes of Davies Dome and Whisky Glacier (James Ross Island, Antarctic Peninsula) in

1979–2006: Journal of Glaciology, 58, no. 111, 904-914.

Esser, R.P., P.R. Kyle, and W.C. McIntosh, McIntosh William C. 2004. 40Ar/39Ar dating of the eruptive history of Mount Erebus, Antarctica: Volcano evolution. Bulletin of Volcanology 66: 671–86. https://doi.org/10.1007/s00445-004-0354-x.

Falconer, T.; Pyne, A.; Wilson, D.; Levy, R.; Nielsen, S.; Petrushak, S. Operations overview for the ANDRILL Southern McMurdo Sound Project, Antarctica. Terra Antart. 2008, 15, 41–48.

Ferrians, O.J., R.J. Kachadoorian, and G.W. Greene, 1969, Permafrost and related engineering problems in Alaska: US Geological Survey Professional Paper 678, p. 37.

Fisher, A.T., K.D. Mankoff, S.M. Tulaczyk, S.W. Tyler, and N. Foley. 2015. High geothermal heat flux measured below the West Antarctic Ice sheet. Science Advances 1, no. 6: e1500093.

Foged N., P.A. Marker, A.V. Christiansen, P. Bauer-Gottwein, F. Jørgensen, A.-S. Høyer, and E. Auken, 2014, Large-scale 3-D modeling by integration of resistivity models and borehole data through inversion: Hydrology and Earth System Science, 18, 4349-4362.

Foged, N., E. Auken, A.V. Christiansen, and K.I. Sørensen, 2013, Test site calibration and validation of airborne and ground based TEM systems: Geophysics, 78, no. 2, E95–E106.

Foley, N., S. Tulaczyk, E. Auken, C. Schamper, H. Dugan, J. Mikucki, R. Virginia, and P. Doran. 2015. Helicopter-borne transient electromagnetics in high-latitude environments: An application in the McMurdo Dry Valleys, Antarctica. Geophysics 81: WA87–99. doi:10.1190/geo2015-0186.1.

Foley, N., S.M. Tulaczyk, D. Grombacher, P.T. Doran, J. Mikucki, K.F. Myers, et al. 2019. Evidence for pathways of concentrated submarine groundwater discharge in East Antarctica from helicopter-borne electrical resistivity measurements. Hydrology 6, no. 2: 54. https://doi.org/10.3390/hydrology6020054.

Frederick, J.M.; Buffett, B.A. Effects of submarine groundwater discharge on the present-day extent of relict submarine permafrost and gas hydrate stability on the Beaufort Sea continental shelf. J. Geophys. Res. Earth Surf. 2015, 120, 417–432.

Freeze, R.A.; Cherry, J.A. Groundwater; Prentice-Hall: New York, NY, USA, 1979; ISBN 0-13-365312-9.

Fukui, K., T. Sone, J.A. Strelin, C.A. Torielli, J. Mori, and Y. Fujii, 2008, Dynamics and GPR stratigraphy of a polar rock glacier on James Ross Island, Antarctic

Peninsula, Journal of Glaciology, 54, no. 186, 445-451.

Gerringa, L.J.A.A.; Alderkamp, A.-C.; Laan, P.; Thuróczy, C.-E.; De Baar, H.J.W.W.; Mills, M.M.; van Dijken, G.L.; Haren, H. van; Arrigo, K.R. Iron from melting glaciers fuels the phytoplankton blooms in Amundsen Sea (Southern Ocean): Iron biogeochemistry. Deep Sea Res. Part II Top. Stud. Oceanogr. 2012, 71–76, 16–31.

Gilichinsky, D., E. Rivkina, V. Shcherbakova, K. Laurinavichuis, and J. Tiedje, 2003, Supercooled water brines within permafrost-an unknown ecological niche for microorganisms: a model for astrobiology: Astrobiology, 3, no. 2, 331-341.

Gosselin, D.C.; Harvey, F.E.; Frost, C.D. Geochemical evolution of ground water in the Great Plains (Dakota) Aquifer of Nebraska: Implications for the management of a regional aquifer system. Groundwater 2001, 39, 98–108.

Green, W.J.; Stage, B.R.; Preston, A.; Wagers, S.; Shacat, J.; Newell, S. Geochemical processes in the Onyx River, Wright Valley, Antarctica: Major ions, nutrients, trace metals. Geochim. Cosmochim. Acta 2005, 69, 839–850.

Haas, C., J. Lobach, S. Hendricks, L. Rabenstein, and A. Pfaffling. 2009. Helicopter-borne measurements of sea ice thickness, using a small and lightweight, digital EM system. Journal of Applied Geophysics 67: 234–41.

Hall, B.L., Denton, G.H., and Hendy, C.H., 2000, Evidence from Taylor Valley for a grounded ice sheet in the Ross Sea, Antarctica: Geografiska Annaler: Series A, Physical Geography, v. 82, p. 275–303.

Hall, B.L.; Baroni, C.; Denton, G.H. Holocene relative sea-level history of the Southern Victoria Land Coast, Antarctica. Glob. Planet. Change 2004, 42, 241–263.

Harpel, C.J., P.R. Kyle, R.P. Esser, W.C. McIntosh, and D.A. Caldwell. 2004. 40Ar/39Ar dating of the eruptive history of Mount Erebus, Antarctica: Summit flows, tephra, and caldera collapse. Bulletin of Volcanology 66, no. 8: 687–702.

Hartlieb, P., M. Toifl, F. Kuchar, R. Meisels, and T. Antretter. 2016. Thermo-physical properties of selected hard rocks and their relation to microwave-assisted comminution. Minerals Engineering 91: 34–41.

Hauck, C., M. Guglielmin, K. Isaksen, and D. Vonder Mühll. 2001. Applicability of frequency-domain and time-domain electromagnetic methods for mountain permafrost studies. Permafrost and Periglacial Processes 12, no. 1: 39–52. https://doi.org/10.1002/ppp.383.

Hazen, A. Some physical properties of sands and gravels. Mass. State Board of

Health. 24th Annu. Rep. 1892, 539–556.

Hendy, C.H. Late Quaternary Lakes in the McMurdo Sound Region of Antarctica. Geogr. Ann. Ser. A Phys. Geogr. 2004, 82, 411–432.

Herut, B., A. Starinsky, A. Katz, and A. Bein, 1990, The role of seawater freezing in the formation of subsurface brines: Geochimica et Cosmochimica Acta, 54, no. 1, 13–21.

Hill, G., P.E. Wannamaker, J.A. Stodt, M.J. Unsworth, V. Maris, P. Bedrosian, E. Wallin, et al. 2017. Imaging the magmatic system of Erebus volcano, Antarctica using the magnetotelluric method. In American Geophysical Union, Fall Meeting 2017, abstract #T22D-08. Retrieved from http://adsabs.harvard.edu/abs/2017AGUFM.T22D..08H.

Hochstein, M. 1967. Electrical Resistivity Measurements on Ice Sheets. Journal of Glaciology 6, 623–633.

Holt, J.W., M.E. Peters, S.D. Kempf, D.L. Morse, and D.D. Blankenship, 2006, Echo source discrimination in single-pass airborne radar sounding data from the Dry Valleys, Antarctica: Implications for orbital sounding of Mars: Journal of Geophysical Research E: Planets, 111, no. E6, E06S24.

Horai, K. 1991. Thermal conductivity of Hawaiian basalt: A new interpretation of Robertson and Peck's data. Journal of Geophysical Research: Solid Earth. 96 (B3): 4125–32. doi:10.1029/90JB02452.

Horai, K., and G. Simmons. 1969. Thermal conductivity of rock-forming minerals. Earth and Planetary Science Letters 6, no. 5: 359–68. https://doi.org/10.1016/0012-821X(69)90186-1.

Hubbard, A., W. Lawson, B. Anderson, B. Hubbard, and H. Blatter, 2004, Evidence for subglacial ponding across Taylor Glacier, Dry Valleys, Antarctica: Annals of Glaciology, 39, no. 1, 79-84.

IPCC, 2007: Climate Change 2007: The Physical Science Basis. Contribution of Working Group I to the Fourth Assessment Report of the Intergovernmental Panel on Climate Change [Solomon, S., D. Qin, M. Manning, Z. Chen, M. Marquis, K.B. Averyt, M.Tignor and H.L. Miller (eds.)]. Cambridge University Press, Cambridge, United Kingdom and New York, NY, USA.

Isaksen,K., R.S. Ødegård, Eiken T., and J.L. Sollid, 2000, Composition, flow and development of two tongue-shaped rock glaciers in the permafrost of Svalbard,

Permafrost and periglacial processes, 11, no. 3, 241-257.

Jørgensen, F., W. Scheer, S. Thomsen, T.O. Sonnenborg, K. Hinsby, H. Wiederhold, C. Schamper, T. Burschil, B. Roth, R. Kirsch, and E. Auken, 2012, Transboundary geophysical mapping of geological elements and salinity distribution critical for the assessment of future sea water intrusion in response to sea level rise: Hydrology and Earth System Science, 16, no. 7, 1845-1862.

Joughin, I., R.B. Alley, and D.M. Holland, 2012, Ice-sheet response to oceanic forcing: Science (New York, N.Y.), 338, no. 6111, 1172-1176.

Joughin, I.R.; Tulaczyk, S.; Engelhardt, H.F. Basal melt beneath Whillans Ice Stream and Ice Streams A and C, West Antarctica. Ann. Glaciol. 2003, 36, 257–262.

Kamb, B., 1987, Glacier surge mechanism based on linked cavity configuration of the basal water conduit system: Journal of Geophysical Research, 92, no. B9, 9083-9100.

Kavanaugh, J.L., and Cuffey, K.M., 2009, Dynamics and mass balance of Taylor Glacier, Antarctica: 2. Force balance and longitudinal coupling: Journal of Geophysical Research, v. 114, p. F04011, doi: 10.1029/2009JF001329.

Keys, J., 1979, Saline discharge at the terminus of the Taylor Glacier: Antarctic Journal of the United States, 1-4.

Kim, M.-J.; Nriagu, J.; Haack, S. Arsenic species and chemistry in groundwater of southeast Michigan. Environ. Pollut. 2002, 120, 379–390.

Kirkegaard, C., and E. Auken, 2015, A parallel, scalable and memory efficient inversion code for very large-scale airborne EM surveys: Geophysical Prospecting, 63, no. 2, 495-507.

Kirkegaard, C., T.O. Sonnenborg, E. Auken, and F. Jørgensen, 2011, Salinity distribution in heterogeneous coastal aquifers mapped by airborne electromagnetics. Vadose Zone Journal, 10, no. 1, 125-135.

Kirsch R., K.-P. Sengpiel, and W. Voss, 2003, The use of electrical conductivity mapping in the definition of an aquifer vulnerability index: Near Surface Geophysics, 1, no. 1, 13-19.

Kirsch, R. 2009. Groundwater geophysics – A tool for hydrogeology. 2nd ed. Berlin: Springer-Verlag.

Korhonen, K., T. Ruskeeniemi, M. Paananen, and J. Lehtimäki. 2009. Frequency domain electromagnetic soundings of Canadian deep permafrost. Geophysica 45, no.

1–2: 77–92.

Kovacs, A., and J.S. Holladay. 1990. Sea-ice thickness measurement using a small airborne electromagnetic sounding system. Geophysics 55, no. 10: 1327–37.

Kwon, E.Y.; Kim, G.; Primeau, F.; Moore, W.S.; Cho, H.-M.; DeVries, T.; Sarmiento, J.L.; Charette, M.A.; Cho, Y.-K. Global estimate of submarine groundwater discharge based on an observationally constrained radium isotope model. Geophys. Res. Lett. 2014, 41, 8438–8444.

Kyle, P.R. 1990. Geothermal resources of Antarctica. Mineral Resources Potential of Antarctica 51: 117–23.

Lachenbruch, A.H., J.H. Sass, B.V. Marshall, and T.H. Moses Jr. 1982. Permafrost, heat flow, and the geothermal regime at Prudhoe Bay, Alaska. Journal of Geophysical Research: Solid Earth 87, no. B11: 9301–16.

Lecher, A. Groundwater Discharge in the Arctic: A Review of Studies and Implications for Biogeochemistry. Hydrology 2017, 4, 41.

Lecher, A.L.; Chien, C.-T.; Paytan, A. Submarine groundwater discharge as a source of nutrients to the North Pacific and Arctic coastal ocean. Mar. Chem. 2016, 186, 167–177.

Lecher, A.L.; Kessler, J.; Sparrow, K.; Garcia-Tigreros Kodovska, F.; Dimova, N.; Murray, J.; Tulaczyk, S.; Paytan, A. Methane transport through submarine groundwater discharge to the North Pacific and Arctic Ocean at two Alaskan sites. Limnol. Oceanogr. 2016, 61, S344–S355.

Levy, J. How big are the McMurdo Dry Valleys? Estimating ice-free area using Landsat image data. Antarct. Sci. 2013, 25, 119–120.

Levy, J.S., A.G. Fountain, M.N. Gooseff, K.A. Welch, and W.B. Lyons, 2011, Water tracks and permafrost in Taylor Valley, Antarctica: Extensive and shallow groundwater connectivity in a cold desert ecosystem: Geological Society of America Bulletin, 123, no. 11-12, 2295-2311.

Li, L.; Barry, D.A.; Stagnitti, F.; Parlange, J.-Y. Submarine groundwater discharge and associated chemical input to a coastal sea. Water Resour. Res. 1999, 35, 3253–3259.

Lyons, B.W.; Frape, S.K.; Welch, K.A. History of McMurdo Dry Valley lakes, Antarctica, from stable chlorine isotope data. Geology 1999, 27, 527.

Lyons, W.B., K.A. Welch, G. Snyder, J. Olesik, E.Y. Graham, G.M. Marion, and R.J.

Poreda, 2005, Halogen geochemistry of the McMurdo dry valleys lakes, Antarctica: Clues to the origin of solutes and lake evolution: Geochimica et Cosmochimica Acta, 69, no. 2, 305-323.

Lyons, W.B.; Mikucki, J.A.; German, L.A.; Welch, K.A.; Welch, S.A.; Gardner, C.B.; Tulaczyk, S.M.; Pettit, E.C.; Kowalski, J.; Dachwald, B. The Geochemistry of Englacial Brine from Taylor Glacier, Antarctica. J. Geophys. Res. Biogeosci. 2019, 124, 633–648.

Lyons, W.B.B.; Tyler, S.W.W.; Wharton, R.A.A.; McKnight, D.M.M.; Vaughn, B.H.H. A Late Holocene desiccation of Lake Hoare and Lake Fryxell, McMurdo Dry Valleys, Antarctica. Antarct. Sci. 1998, 10, 247–256.

Mackay, S.L., Marchant, D.R., Lamp, J.L., and Head, J.W., 2014, Cold-based debris-covered glaciers: Evaluating their potential as climate archives through studies of ground-penetrating radar and surface morphology: Journal of Geophysical Research: Earth Surface, v. 119, p. 1–36, doi: 10.1002/2014JF003178.Received.

Mahowald, N.M.; Baker, A.R.; Bergametti, G.; Brooks, N.; Duce, R.A.; Jickells, T.D.; Kubilay, N.; Prospero, J.M.; Tegen, I. Atmospheric global dust cycle and iron inputs to the ocean. Global Biogeochem. Cycles 2005, 19, doi:10.1029/2004GB002402.

Martin, J.H.; Gordon, R.M.; Steve, E.F.; Fitzwater, S.E. Iron in Antarctic waters. Nature 1990, 345, 156–158.

McGinnis, L. D., D. R. Osby, and R. Kohout, 1982, Paleohydrology inferred from salinity measurements on Dry Valley Drilling Project cores from Taylor Valley, Antarctica:, p. 1133–1138. In C. Craddock [ed.], Antarctic Geoscience.

McGinnis, L., K. Nakao, and C. Clark, 1973, Geophysical identification of frozen and unfrozen ground, Antarctica (Sanger, Ed.): Proceedings 2nd International Conference on Permafrost.

McGinnis, L.D. Artesian well at Don Juan Pond. Antarct. J. US 1979, 14, 26–27.

McGinnis, L.D., and D.R. Osby, 1977, Logging summary of Dry Valley drilling project: Antartica Journal of the United States , 12, 115-117.

McGinnis, L.D., and T.E. Jensen, 1971, Permafrost-Hydrogeologic Regimen in Two Ice-Free Valleys, Antarctica, from Electrical Depth Sounding: Quaternary Research, 1, no. 3, 389-409.

McGinnis, L.D.; Jensen, T.E. Permafrost-Hydrogeologic Regimen in Two Ice-Free

Valleys, Antarctica, from Electrical Depth Sounding. Quat. Res. 1971, 409, 389–409.

McGinnis, L.D.; Stuckless, J.S.; Osby, D.R.; Kyle, P.R. Gamma Ray, Salinity, and Electric Logs of DVDP Boreholes. Dry Val. Drill. Proj. 1981, 33, 95–108.

McGuire, A.D., L.G. Anderson, T.R. Christensen, S. Dallimore, L.D. Guo, D.J. Hayes, M. Heimann, T.D. Lorenson, R.W. Macdonald, and N. Roulet, 2009, Sensitivity of the carbon cycle in the Arctic to climate change: Ecological Monographs, 79, no. 4, 523-555.

McKay, C.P.; Hand, K.P.; Doran, P.T.; Andersen, D.T.; Priscu, J.C. Clathrate formation and the fate of noble and biologically useful gases in Lake Vostok, Antarctica. Geophys. Res. Lett. 2003, 30, doi:10.1029/2003GL017490.

McKelvey, B. C., 1975, DVDP sites 10 and 11, Taylor Valley, p. 16–60. In M.G. Mudrey Jr. and L.D. McGinnis [eds.], Dry Valley Drilling Project Bulletin 5.

McKenzie, J.M., and C.I. Voss. 2013. Permafrost thaw in a nested groundwater-flow system. Hydrogeology Journal 21, no. 1: 299–316.

Melles, M., J. Brigham-Grette, P. Minyuk, C. Koeberl, A. Andreev, T. Cook, G. Fedorov, et al. 2011. The Lake El'gygytgyn scientific drilling project–conquering arctic challenges through continental drilling. Scientific Drilling 11: 29–40.

Michaud, A.B.; Dore, J.E.; Achberger, A.M.; Christner, B.C.; Mitchell, A.C.; Skidmore, M.L.; Vick-Majors, T.J.; Priscu, J.C. Microbial oxidation as a methane sink beneath the West Antarctic Ice Sheet. Nat. Geosci. 2017, 10, 582–586.

Mikucki, J. A, and Priscu, J.C., 2007, Bacterial diversity associated with Blood Falls, a subglacial outflow from the Taylor Glacier, Antarctica.: Applied and Environmental Microbiology, v. 73, p. 4029–39, doi: 10.1128/AEM.01396-06.

Mikucki, J.A., A. Pearson, D.T. Johnston, A.V. Turchyn, J. Farquhar, D.P. Schrag, A.D. Anbar, J.C. Priscu, and P.A. Lee, 2009, A contemporary microbially maintained subglacial ferrous "ocean": Science, 324, no. 5925, 397-400.

Mikucki, J.A., C.C.M. Foreman, B. Sattler, W.B. Lyons, and J.C. Priscu, 2004, Geomicrobiology of Blood Falls: An iron-rich saline discharge at the terminus of the Taylor Glacier, Antarctica: Aquatic Geochemistry, 10, no. 3-4, 199-220.

Mikucki, J.A., E. Auken, S. Tulaczyk, R.A. Virginia, C. Schamper, K.I. Sørensen, P.T. Doran, H. Dugan, and N. Foley. 2015. Deep groundwater and potential subsurface habitats beneath an Antarctic dry valley. Nature Communications 6: 6831.

doi:10.1038/ncomms7831.

Minsley, B.J., J.D. Abraham, B.D. Smith, J.C. Cannia, C.I. Voss, M.T. Jorgenson, M.A. Walvoord, B.K. Wylie, L. Anderson, L.B. Ball, M. Deszcz-Pan, T.P. Wellman, and T.A. Ager, 2012, Airborne electromagnetic imaging of discontinuous permafrost: Geophysical Research Letters, 39, no. 2., 8 p.

Monaghan, A.J., D.H. Bromwich, J.G. Powers, and K.W. Manning. 2005. The climate of the McMurdo, Antarctica, region as represented by one year of forecasts from the Antarctic mesoscale prediction system. Journal of Climate 18, no. 8: 1174–89.

Moore, J.K.; Abbott, M.R. Phytoplankton Chlorophyll Distributions and Primary Production in the Southern Ocean. J. Geophys. Res. 2000, 105, 28709–28722, doi:10.1029/1999JC000043.

Moore, W.S. The Effect of Submarine Groundwater Discharge on the Ocean. Ann. Rev. Mar. Sci. 2009, 2, 59–88.

Morin, R.H., T. Williams, S.A. Henrys, D. Magens, F. Niessen, and D. Hansaraj. 2010. Heat flow and hydrologic characteristics at the AND-1B borehole, ANDRILL McMurdo Ice Shelf Project, Antarctica. Geosphere 6, no. 4: 370–8.

Multala, J., H. Hautaniemi, M. Oksama, M. Lepparanta, J. Haapala, A. Herlevi, K. Riska, and M. Lensu. 1996. An airborne electromagnetic system on a fixed wing aircraft for sea ice thickness mapping. Cold Regions Science and Technology 24, no. 4: 355–73.

Nichols, R. L., and D. G. Ball. 1964. Four-fold check on mean annual temperature, McMurdo Sound, Antarctica. Journal of Glaciology 5, 353–355.

Null, K.A.; Reide Corbett, D.; Crenshaw, J.; Peterson, R.N.; Peterson, L.E.; Lyons, W.B. Groundwater discharge to the western Antarctic coastal ocean. Polar Res. 2019, 38, doi:10.33265/polar.v38.3497.

Osterkamp, T., and M. Jorgenson, 2009, Permafrost conditions and processes: Young, R., and Norby, L., Geological Monitoring: Boulder, Colorado, Geological Society of America, 205-227.

Osterkamp, T.E., and C.R. Burn. 2003. Permafrost. In Encyclopedia of atmospheric sciences, ed. J.R. Holton, J.Pyle, and J.A. Curry, 1717–29. Oxford, UK: Academic Press.

Palacky, G.J., 1987, Clay mapping using electromagnetic methods: First Break, 5, no.

8, 295-306.

Palacky, G.V. 1987. Resistivity characteristics of geologic targets. Electromagnetic Methods in Applied Geophysics 1 (Theory): 1351.

Parmelee, D.E., P.R. Kyle, M.D. Kurz, S.M. Marrero, and F.M. Phillips. 2015. A new Holocene eruptive history of Erebus volcano, Antarctica using cosmogenic 3He and 36Cl exposure ages. Quaternary Geochronology 30: 114–31.

Pattyn, F. Antarctic subglacial conditions inferred from a hybrid ice sheet/ice stream model. Earth Planet. Sci. Lett. 2010, 295, 451–461.

Paytan, A., A.L. Lecher, N. Dimova, K.J. Sparrow, F.G.-T. Kodovska, J. Murray, S. Tulaczyk, and J.D. Kessler, 2015, Methane transport from the active layer to lakes in the Arctic using Toolik Lake, Alaska, as a case study: Proceedings of the National Academy of Sciences , doi: 10.1073/pnas.1417392112 .

Pettit, E.C., E.N. Whorton, E.D. Waddington, and R.S. Sletten, 2014, Influence of debris-rich basal ice on flow of a polar glacier: Journal of Glaciology 60, no. 223: 989-1006.

Pfaffling, A., C. Haas, and J.E. Reid. 2007. Direct helicopter EM—Sea-ice thickness inversion assessed with synthetic and field data. Geophysics 72, no. 4: F127–37. https://doi.org/10.1190/1.2732551.

Poreda, R.J., A.G. Hunt, W.B. Lyons, and K.A. Welch, 2004, The helium isotopic chemistry of Lake Bonney, Taylor Valley, Antarctica: Timing of late holocene climate change in Antarctica: Aquatic Geochemistry, 10, no. 3-4, 353-371.

Powell, R.D., 1981, Sedimentation Conditions in Taylor Valley, Antarctica, Inferred from Textural Analysis of DVDP Cores: Dry Valley Drilling Project, American Geophysical Union, 331-349.

Prieto, C.; Destouni, G. Quantifying hydrological and tidal influences on groundwater discharges into coastal waters. Water Resour. Res. 2005, 41, doi:10.1029/2004WR003920.

Priscu, J.C.; Tulaczyk, S.; Studinger, M.; Kennicutt II, M.C.; Christner, B.C.; Foreman, C.M. Antarctic subglacial water: Origin, evolution, and ecology. In Polar Lakes and Rivers; Oxford University Press: Oxford, England, 2008; ISBN 9780199213887.

Rack, W., C. Haas, and P.J. Langhorne. 2013. Airborne thickness and freeboard measurements over the McMurdo Ice Shelf, Antarctica, and implications for ice density. Journal of Geophysical Research: Oceans 118, no. 11: 5899–907.

https://doi.org/10.1002/2013JC009084.

Ragnarsson, Á. 2003. Utilization of geothermal energy in Iceland. In International geothermal conference, Reykjavik, September 2003, paper 123, 39–45.

Raiswell, R.; Benning, L.G.; Tranter, M.; Tulaczyk, S. Bioavailable iron in the Southern Ocean: The significance of the iceberg conveyor belt. Geochem. Trans. 2008, 9, 7.

Recktenwald, G.W. 2004. Finite-difference approximations to the heat equation. Mechanical Engineering 10: 1–27.

Risk, G.F., and M.P. Hochstein. 1974. Heat flow at arrival heights, Ross Island, Antarctica. New Zealand Journal of Geology and Geophysics 17, no. 3: 629–44.

Ruotoistenmäki, T., and J. Lehtimäki. 1997. Estimation of permafrost thickness using ground geophysical measurements, and its usage for defining vertical temperature variations in continental ice and underlying bedrock. Journal of Glaciology 43, 359–364.

Salarashayeri, A.F.; Siosemarde, M. Prediction of soil hydraulic conductivity from particle-size distribution. World Acad Sci Eng Technol 2012, 61, 454–458.

Santos, I.R.; Eyre, B.D.; Huettel, M. The driving forces of porewater and groundwater flow in permeable coastal sediments: A review. Estuar. Coast. Shelf Sci. 2012, 98, 1–15.

Schamper, C., E. Auken, and K.I. Sørensen, 2014, Coil response inversion for very early time modeling of helicopter-borne time-domain EM data and mapping of near-surface geological layers: Geophysical Prospecting, 62, no. 3, 658-674

Shean, D.E., and D.R. Marchant, 2010, Seismic and GPR surveys of Mullins Glacier, Mcmurdo Dry Valleys, Antarctica: Ice thickness, internal structure and implications for surface ridge formation: Journal of Glaciology, 56, no. 195, 48-64.

Simmons, G.M. Importance of submarine groundwater discharge (SGWD) and seawater cycling to material flux across sediment/water interfaces in marine environments. Mar. Ecol. Prog. Ser. 1992, 84, 173–184.

Skidmore, M.; Tranter, M.; Tulaczyk, S.; Lanoil, B. Hydrochemistry of ice stream beds-Evaporitic or microbial effects? Hydrol. Process. 2010, 24, 517–523.

Slomp, C.P.; Van Cappellen, P. Nutrient inputs to the coastal ocean through submarine groundwater discharge: controls and potential impact. J. Hydrol. 2004,

295, 64–86.

Smith, R., 2014, Electromagnetic induction methods in mining geophysics from 2008 to 2012: Surveys in Geophysics, 35, no. 1, 123-156.

Sold, L., M. Huss, A. Eichler, M. Schwikowski, and M. Hoelzle, 2014, Recent accumulation rates of an alpine glacier derived from firn cores and repeated helicopter-borne GPR, The Chryosphere Discussion, 8, 4431-4462.

Sørensen, K.I., and E. Auken, 2004, SkyTEM — A new high-resolution helicopter transient electromagnetic system: Exploration Geophysics, 35, no. 3, 194-202.

Sørensen, K.I.; Auken, E. SkyTEM—A new high-resolution transient electromagnetic system. Explor. Geophys. 2004, 35, 191–199.

Spigel, R.H., J.C. Priscu, 1996, Evolution of temperature and salt structure of Lake Bonney, a chemically stratified Antarctic lake: Hydrobiologia , 321, no. 3, 177-190.

Starinsky, A., and A. Katz, 2003, The formation of natural cryogenic brines: Geochimica et Cosmochimica Acta, 67, no. 8, 1475-1484.

Steuer, A., B. Siemon, and E. Auken. 2009. A comparison of helicopter-borne electromagnetics in frequency- and time-domain at the Cuxhaven valley in Northern Germany. Journal of Applied Geophysics 67, no. 3: 194–205. https://doi.org/10.1016/j.jappgeo.2007.07.001.

Stuiver, M., I.C. Yang, G.H. Denton, and T.B. Kellogg, 1981, Oxygen isotope ratios of Antarctic permafrost and glacier ice: Dry Valley Drilling Project (ed L. D. Mcginnis), American Geophysical Union, Washington, D. C.

Sugden, D., G. Denton, and D. Marchant, 1995, Landscape evolution of the Dry Valleys, Transantarctic Mountains: Tectonic implications: Journal of Geophysical Research, 100, no. B6, 9949-9967.

Teatini, P., L. Tosi, A. Viezzoli, L. Baradello, M. Zecchin, S. Silvestri, 2011, Understanding the hydrogeology of the Venice Lagoon subsurface with airborne electromagnetics: Journal of Hydrology, 411, no. 3-4, 342-354.

Thuróczy, C.-E.; Alderkamp, A.-C.; Laan, P.; Gerringa, L.J.A.; Mills, M.M.; Van Dijken, G.L.; De Baar, H.J.W.; Arrigo, K.R. Key role of organic complexation of iron in sustaining phytoplankton blooms in the Pine Island and Amundsen Polynyas (Southern Ocean). Deep Sea Res. Part II Top. Stud. Oceanogr. 2012, 71–76, 49–60.

Todd, B.J., and S.R. Dallimore. 2002. Electromagnetic and geological transect across

permafrost terrain, Mackenzie River delta, Canada. Geophysics 63, 1914–24.

Toner, J.D., and R.S. Sletten, 2013, The formation of Ca-Cl-rich groundwaters in the Dry Valleys of Antarctica: Field measurements and modeling of reactive transport: Geochimica et Cosmochimica Acta, 110, no. 1, 84-105.

Toner, J.D., R.S. Sletten, and M.L. Prentice, 2013, Soluble salt accumulations in Taylor Valley, Antarctica: Implications for paleolakes and Ross Sea Ice Sheet dynamics: Journal of Geophysical Research: Earth Surface, 118, no. 1, 198-215.

Torii, T., and N. Yamagata, 1981, Limnological Studies of Saline Lakes in the Dry Valleys: Dry Valley Drilling Project (ed L. D. Mcginnis), American Geophysical Union, Washington, D. C.

Tréguer, P.; Jacques, G. Dynamics of nutrient and phytoplankton and cycles of carbon, nitrogen and silicon in the Southern Ocean: a review. Polar Biol 1992, 12, 149–162.

Tréguer, P.J. The Southern Ocean silica cycle. Comptes Rendus - Geosci. 2014, 346, 279–286.

Tulaczyk, S., J.A. Mikucki, M.R. Siegfried, J.C. Priscu, C.G. Barcheck, L.H. Beem, A. Behar, et al. 2014. WISSARD at Subglacial Lake Whillans, West Antarctica: scientific operations and initial observations. Annals of Glaciology 55, no. 65: 51–8.

Uemura, T.; Taniguchi, M.; Shibuya, K. Submarine groundwater discharge in Lützow-Holm Bay, Antarctica. Geophys. Res. Lett. 2011, 38, doi:10.1029/2010GL046394.

Viezzoli, A., A.V. Christiansen, E. Auken, and K. Sørensen. 2008. Quasi-3D modeling of airborne TEM data by spatially constrained inversion. Geophysics 73, no. 3: F105–13.

Vignoli, G., G. Fiandaca, A.V. Christiansen, C. Kirkegaard, and E. Auken, 2015, Sharp spatially constrained inversion with applications to transient electromagnetic data: Geophysical Prospecting, 63, no. 1, 243-255.

Wadham, J.L., M. Tranter, S. Tulaczyk, and M. Sharp, 2008, Subglacial methanogenesis: A potential climatic amplifier?: Global Biogeochemical Cycles, 22, no.2, 1-16.

Wadham, J.L., R. De'ath, F.M. Monteiro, M. Tranter, A. Ridgwell, R. Raiswell, and S. Tulaczyk, 2013, The potential role of the Antarctic Ice Sheet in global biogeochemical cycles: Earth and Environmental Science Transactions of the Royal

Society of Edinburgh, 104, no.1, 55-67.

Wadham, J.L., S. Arndt, S. Tulaczyk, M. Stibal, M. Tranter, J. Telling, G.P. Lis, E. Lawson, A. Ridgwell, A. Dubnick, M.J. Sharp, A.M. Anesio, and C.E.H. Butler, 2012, Potential methane reservoirs beneath Antarctica: Nature, 488, 633-637.

Wadham, J.L.; De'ath, R.; Monteiro, F.M.; Tranter, M.; Ridgwell, A.; Raiswell, R.; Tulaczyk, S. The potential role of the Antarctic Ice Sheet in global biogeochemical cycles. Earth Environ. Sci. Trans. R. Soc. Edinburgh 2013, 104, 55–67.

Wadham, J.L.; Tranter, M.; Skidmore, M.; Hodson, A.J.; Priscu, J.; Lyons, W.B.; Sharp, M.; Wynn, P.; Jackson, M. Biogeochemical weathering under ice: Size matters. Global Biogeochem. Cycles 2010, 24, 3025.

Wallace, J., and P. Hobbs. 2006. Atmospheric science: An introductory survey. 483 pp. Burlington, Mass: Academic Press.

Wannamaker, P. E., J. A. Stodt, L. Pellerin, S. L. Olsen, and D. B. Hall. 2004. Structure and thermal regime beneath the South Pole region, East Antarctica, from magnetotelluric measurements. Geophysical Journal International 157, 36–54.

Wannamaker, P., G. Hill, J. Stodt, V. Maris, Y. Ogawa, K. Selway, G. Boren, E. Bertrand, D. Uhlmann, B. Ayling, A. M. Green, and D. Feucht. 2017. Uplift of the central transantarctic mountains. Nature Communications 8, 1588.

Ward S.H., and G.W. Hohmann, 1988, Chapter 4: Electromagnetics theory for geophysical applications. In: Investigations in geophysics No.3: Electromagnetics methods in applied geophysics (vol. 1, Theory), Nabighian M.N. (ed.).

Willis, M.J., B.G. Herried, M.G. Bevis, and R.E. Bell, 2015, Recharge of a subglacial lake by surface meltwater in northeast Greenland: Nature, 518, 223-227.

Winberry, J.P., S. Anandakrishnan, D.A. Wiens, R.B. Alley, and K. Christianson, 2011, Dynamics of stick–slip motion, Whillans Ice Stream, Antarctica: Earth and Planetary Science Letters, 305, no. 3-4, 283-289.

Worby, A., P. Griffin, V. Lytle, and R. Massom. 1999. On the use of electromagnetic induction sounding to determine winter and spring sea ice thickness in the Antarctic. Cold Regions Science and Technology 29, no. 1: 49–58. https://doi.org/10.1016/S0165-232X(99)00003-8.

Zhdanov, S.M. 2017. Airborne electromagnetic methods. In Foundations of geophysical electromagnetic theory and methods, 663–81. Elsevier.

https://doi.org/10.1016/b978-0-44-463890-8.00020-7.

Zimov, S., E. Schuur, and F. Chapin, 2006, Permafrost and the global carbon budget: Science, 312, 1612–1613.